

NASA Technical Memorandum 4500

Extraction of Stability and Control Derivatives From Orbiter Flight Data

Kenneth W. Iliff and Mary F. Shafer

JUNE 1993



NASA Technical Memorandum 4500

Extraction of Stability and Control Derivatives From Orbiter Flight Data

Kenneth W. Iliff and Mary F. Shafer
Dryden Flight Research Facility
Edwards, California



National Aeronautics and
Space Administration
Office of Management
Scientific and Technical
Information Program
1993

EXTRACTION OF STABILITY AND CONTROL DERIVATIVES FROM ORBITER FLIGHT DATA

Kenneth W. Iliff and Mary F. Shafer
NASA Dryden Flight Research Facility
Edwards, California

SUMMARY

The Space Shuttle Orbiter has provided unique and important information on aircraft flight dynamics. This information has provided the opportunity to assess the flight-derived stability and control derivatives for maneuvering flight in the hypersonic regime. In the case of the Space Shuttle Orbiter, these derivatives are required to determine if certain configuration placards (limitations on the flight envelope) can be modified. These placards were determined on the basis of preflight predictions and the associated uncertainties. As flight-determined derivatives are obtained, the placards are reassessed, and some of them are removed or modified. Extraction of the stability and control derivatives was justified by operational considerations and not by research considerations. Using flight results to update the predicted database of the orbiter is one of the most completely documented processes for a flight vehicle. This process followed from the requirement for analysis of flight data for control system updates and for expansion of the operational flight envelope. These results show significant changes in many important stability and control derivatives from the preflight database. This paper presents some of the stability and control derivative results obtained from Space Shuttle flights. Some of the limitations of this information are also examined.

INTRODUCTION

In the last 12 yr, the Space Shuttle Orbiter has provided unique and important information concerning aerothermodynamics and aircraft flight dynamics. Maneuvering manned flight over a wide range of hypersonic velocities was demonstrated for the first time. These data have provided the opportunity to assess flight characteristics in completely new flight regimes. Among the flight characteristics to be assessed are the stability and control derivatives.

Estimates of the stability and control derivatives can be used to expand the flight envelope, to update simulators, to enhance maneuvering capability and flying qualities, and to provide the information necessary to improve the flight control system. In the case of the Space Shuttle, these derivatives are required to determine if certain configuration placards (limitations on the flight envelope) can be modified. Many of these placards involve the longitudinal and lateral center-of-gravity (c.g.) limits. The placards were determined on the basis of preflight predictions and the associated uncertainties. As flight-determined derivatives are obtained, the placards are reassessed, and some are removed or modified.

The stability and control maneuvers performed by the Space Shuttle Orbiter were done so that the operational envelope could be safely expanded. Maneuvers were done specifically to update the aerodynamics and the associated uncertainties for Space Shuttle project support and were not done

to provide aerodynamic research information. Lack of research emphasis limits the amount of general information that can be obtained. In spite of these limitations, much information of research value was obtained. At this time, the Space Shuttle has flown 54 flights. This paper presents some of the stability and control derivative results obtained from these Space Shuttle flights. In addition, some of the limitations of the information obtained are examined.

The authors greatly appreciate the conversations and information provided by Mr. Joe Baumbach at Rockwell International Space Division (Rockwell), Downey, California. The plots showing the results of research conducted by four groups of analysts were taken from Rockwell's Internal Letters SAS/AERO/86-062, June 26, 1986, by Mr. J.J. Baumbach and SAS/AERO/86-079, July 16, 1986, by Mr. Alan H. Weiner.

NOMENCLATURE

Abbreviations

ACIP	aerodynamic coefficient identification package
AFFTC	Air Force Flight Test Center, Edwards Air Force Base, California
c.g.	center of gravity
FAD	flight assessment deltas
GPC	general purpose computer
JSC	Johnson Space Center, Houston, Texas
MMLE	maximum likelihood estimation algorithm
NASA-Dryden	Dryden Flight Research Facility, Edwards, California
OI	operational instrumentation
PTI	programmed test input
RCS	reaction control system
STS	Space Transportation System (used with an assigned number to designate a mission)

Symbols

a_n	normal acceleration, g
a_x	longitudinal acceleration, g
a_y	lateral acceleration, g

A, B, C, D, F, G	system matrices
$C_{L_{BF}}$	coefficient of lift due to body flap, deg^{-1}
$C_{l_{RJ}}$	coefficient of rolling moment due to roll jet, per jet
$C_{l_{YJ}}$	coefficient of rolling moment due to yaw jet, per jet
$C_{l_{YJ_2}}$	coefficient of rolling moment due to two yaw jets, per jet
$C_{l_{YJ_4}}$	coefficient of rolling moment due to four yaw jets, per jet
$C_{l_{\beta}}$	coefficient of rolling moment due to angle of sideslip (dihedral effect), deg^{-1}
$C_{l_{\delta_a}}$	coefficient of rolling moment due to differential aileron, deg^{-1}
$C_{l_{\delta_r}}$	coefficient of rolling moment due to rudder, deg^{-1}
$C_{m_{BF}}$	coefficient of pitching moment due to body flap, deg^{-1}
$C_{m_{DJ}}$	coefficient of pitching moment due to down-firing jet, per jet
$C_{m_{YJ_2}}$	coefficient of pitching moment due to two yaw jets, per jet
$C_{m_{\alpha}}$	coefficient of pitching moment due to angle of attack, deg^{-1}
$C_{m_{\delta_e}}$	coefficient of pitching moment due to elevon, deg^{-1}
$C_{m_{\delta_e^2}}$	coefficient of pitching moment due to elevon squared, deg^{-2}
$C_{m_{\delta_{e0}}}$	coefficient of pitching moment due to elevon when quadratic terms are assumed, deg^{-1}
C_{m_0}	pitching moment bias
$C_{N_{DJ}}$	coefficient of normal force due to down-firing jet, per jet
$C_{n_{\beta}}$	coefficient of yawing moment due to angle of sideslip (directional stability), deg^{-1}
$C_{n_{\delta_a}}$	coefficient of yawing moment due to differential elevon, deg^{-1}
$C_{n_{\delta_r}}$	coefficient of yawing moment due to rudder, deg^{-1}
$C_{Y_{YJ}}$	coefficient of side force due to yaw jet, per jet
$C_{Y_{YJ_2}}$	coefficient of side force due to two yaw jets, per jet
$C_{Y_{\beta}}$	coefficient of side force due to angle of sideslip, deg^{-1}
$C_{Y_{\delta_r}}$	coefficient of side force due to rudder, deg^{-1}

f	system state function
GG^*	measurement noise covariance matrix
g	system observation functions
H	approximation to the information matrix
J	cost function
L	iteration number
L_{YJ}	rolling moment due to yaw jet, ft-lbf/jet
M	Mach number
\dot{M}_J/\dot{M}_∞	jet mass flow ratio
N	number of time points
\mathbf{n}	state noise vector
p	roll rate, deg/sec
\dot{p}	roll acceleration, deg/sec ²
q	pitch rate, deg/sec
\dot{q}	pitch acceleration, deg/sec ²
\bar{q}	dynamic pressure, lb/ft ²
r	yaw rate, deg/sec
\dot{r}	yaw acceleration, deg/sec ²
t	time, sec
\mathbf{u}	known control input vector
V	velocity, ft/sec
\mathbf{x}	state vector
$\dot{\mathbf{x}}$	time derivative of state vector
$\tilde{\mathbf{x}}$	predicted state estimate
\mathbf{z}	observation vector
$\tilde{\mathbf{z}}$	predicted Kalman filter estimate
α	angle of attack, deg

β	angle of sideslip, deg
Δ	increment of derivative added to preflight aerodynamic data book value to best represent flight
δ	difference between maneuver estimate and flight-derived derivative fairing
δ_a	differential elevon deflection, deg
δ_e	elevon deflection, deg
δ_r	rudder deflection, deg
η	measurement noise vector
ϕ	transition matrix
ϕ_J/ϕ_∞	jet momentum ratio
ψ	integral of the transition matrix
ξ	unknown parameter vector
$\hat{\xi}$	estimate of ξ

VEHICLE DESCRIPTION

Figure 1 shows the Space Shuttle Orbiter, a large double-delta-winged vehicle designed to enter the atmosphere and land horizontally. This vehicle is 122-ft long with a wingspan of 78 ft. The entry control system consists of 12 vertical reaction control system (RCS) jets (6 down-firing and 6 up-firing), 8 horizontal RCS jets (4 to the left and 4 to the right), 4 elevon surfaces, a body flap, and a split rudder surface.

The vertical jets and the elevons control pitch and roll. These jets and elevons are used symmetrically to control pitch and asymmetrically to control roll. Used as a secondary pitch trim control, the body flap helps maintain the predetermined elevon schedule as a function of flight condition. The rudder and side-firing (yaw) jets provide directional control. The split rudder also functions as the speed brake. The vertical jets operate in roll (roll jets) only for dynamic pressures, \bar{q} , of less than 10 lb/ft² and in pitch (pitch jets) for dynamic pressures less than 40 lb/ft². The yaw jets are active when the Mach number, M , is greater than 1. The body flap and elevons activate at a dynamic pressure of 2 lb/ft². The rudders activate at Mach numbers below 5.

PREDICTIONS

The predicted stability and control derivatives are presented in the preflight aerodynamic data book (ref. 1). These predictions were based on more than 25,000 hr of wind-tunnel testing. In addition to the predicted values of the derivatives, the aerodynamic data book also contains estimates of the uncertainty in the predictions. These preflight uncertainties are called the

variations. These variations are based on the evaluation of previous correlations between wind-tunnel and flight-determined derivatives for similar aircraft. The variations in reference 1 are based, in part, on the study of wind-tunnel and flight correlations presented in reference 2.

ORBITER STABILITY AND CONTROL EXAMPLE

The primary reasons for analyzing the Space Shuttle flight dynamic data are to support expansion of the operational envelope and to improve overall safety of this vehicle. This example shows how these analyses are used in conjunction with the flight program.

The Space Shuttle Orbiter trajectory during reentry and, therefore, its heating profile are controlled through a series of energy-management bank reversals. The vehicle is controlled by conventional aerodynamic surfaces and by the RCS jets. The first bank reversal on the first Space Shuttle flight, STS-1, resulted in a significantly larger response than had been predicted.

Figure 2 shows the response to the automated control inputs computed using the predicted stability and control derivatives. Note that the control inputs shown here (and for all the other simulation comparisons) are the closed-loop commands from the Orbiter control laws. The maneuver was to be made at a velocity, V , of 24,300 ft/sec and at $\bar{q} = 12$ lb/ft².

Figure 3 shows the STS-1 maneuver that occurred at this flight condition and depicts a more hazardous maneuver than was expected. At this flight condition, the excursions must be kept small. This flight maneuver resulted in twice the angle-of-sideslip, β , peaks than were predicted and in a somewhat higher than predicted roll rate. In addition, more yaw jet firing than was anticipated occurred, and the motion was more poorly damped than was predicted.

From comparing the predicted maneuver with the actual maneuver (fig. 4), obviously, the stability and control derivatives were significantly different from those that were predicted. It is fortunate that a conservative control system design philosophy had been used for the Space Shuttle. Although the flight maneuver resulted in excursions greater than planned, the control system did manage to damp out the oscillation in less than 1 min. With a less conservative design approach, the resulting entry maneuver could have been a great deal worse.

To assess the problem with the first bank maneuver, the flight-determined stability and control derivatives were extracted from the measured in-flight vehicle motions and compared with the predictions. Procedures for the stability and control derivative extraction are discussed in the Stability and Control Derivative Extraction section. Of the derivatives obtained from STS-1, the two important ones that differed most from the predictions for the bank maneuver were dihedral effect or coefficient of rolling moment due to angle of sideslip, C_{l_β} , and the rolling moment due to yaw jet firing, L_{YJ} . Because the entry tends to be monotonically decreasing in Mach number, the derivatives are portrayed here as a function of the Mach number derived from the general purpose computer (GPC), or GPC-derived Mach number; that is, $V/1000$.

Figure 5 shows C_{l_β} as a function of GPC-derived Mach number, and figure 6 shows L_{YJ} as a function of GPC-derived Mach number. Only the estimates from STS-1 are shown in these figures. The estimate for this maneuver is shown at Mach 24.

When only the change in C_{l_p} was entered in the simulation database, the maneuver looked very much like the original prediction. As expected, however, the frequency of the oscillations changed and more closely matched the actual flight frequencies.

Figure 7 shows the difference between the preflight simulation with only L_{YJ} changed and the flight response. These two time histories are very close, considering that all other differences between the flight-determined and -predicted derivatives have been ignored.

The primary problem with the initial bank maneuver was the poor prediction of L_{YJ} . The Space Shuttle control system software is very complex and cannot be changed and verified between missions. As a result, an interim approach was taken to keep this large excursion from occurring on future flights. First, the flight-determined derivatives were put into the simulation database. Next, Space Shuttle pilots practiced performing the maneuver manually, trying to attain a smaller response within more desirable limits. Then, the maneuver was performed manually on STS-2 through STS-4.

Figure 8 shows the manually flown maneuver from STS-2. For this maneuver, roll rate, yaw rate, and sideslip angle were within the desired limits. The maneuver does not look like the originally predicted response because the derivatives and input differed, and the basic control system remained unchanged. Because the response variables were kept low and the inputs were slower and smaller, flight responses on STS-2 through STS-4 did not show a tendency to oscillate. The software was updated for STS-5, and the resulting automated maneuver is essentially indistinguishable from that shown in figure 8. This maneuver has been used on all subsequent Space Shuttle flights.

STABILITY AND CONTROL DERIVATIVE EXTRACTION

The general parameter estimation or extraction problem is discussed in reference 3. The parameter estimation technique used for the Space Shuttle, as discussed in the Orbiter Stability and Control Example section, enabled the extraction of the stability and control derivatives from flight data. Although the parameter estimation technique described here was used to extract stability and control derivatives, the same technique applies to any process governed by differential equations, such as heat transfer or other thermal processes.

Key issues in extracting stability and control derivatives from flight data are best categorized into four areas. These areas include the mathematical model; the flight data measurements; the maneuvers or programmed test inputs (PTI's); and the maximum likelihood, or extraction, method. The Space Shuttle is modeled by a set of dynamic equations containing unknown stability and control derivatives. The equations used are those given in reference 4, except that dimensional derivatives are used for RCS jets. The other three areas are discussed in the next three subsections.

Flight Data Measurements

The Space Shuttle flight data used for stability and control derivative estimation were recorded on three onboard systems (ref. 5). The primary data were recorded on the aerodynamic coefficient identification package (ACIP). This package was specifically intended for providing high-quality data at a high sample rate to enhance the stability and control derivative estimates. A second

system recorded data from the onboard GPC to provide the parameters defining the flight condition and the vehicle Euler angles. The third system was the operational instrumentation (OI) system. Time histories of the RCS jet chamber pressure were obtained from this system. These chamber pressures are used because they reflect the thrust buildup and decay. The RCS jet time histories presented in this paper are sums of the active chamber pressures divided by the nominal single chamber pressure, which gives the number of jets firing for nominal conditions. The following list of instrumentation properties gives the data source of the important signals used in the analysis as well as the individual sample rates and measurement resolutions:

Measurement	Sample rate, sample/sec	Source	Resolution	Bits
p	174	ACIP	0.004	14
q, r	174	ACIP	0.001	14
a_x	174	ACIP	0.0002	14
a_y	174	ACIP	0.00006	14
a_n	174	ACIP	0.0004	14
\dot{p}	174	ACIP	0.01	14
\dot{q}, \dot{r}	174	ACIP	0.007	14
Elevons	174	ACIP	0.004	14
Rudder	174	ACIP	0.003	14
Body flap	12.5 ^a	GPC	0.04	10
RCS jets	25	OI	0.004	8
α	1	GPC	---	---
β	5	GPC	---	---
Euler angles	5	GPC	---	---
Flight condition	1	GPC	---	---

^aBody flap sampled at 1 sample/sec on STS-1 and -2.

The resolution of the ACIP parameters allows the analysis of some very small maneuvers. These data from the three sources were corrected for time skew, converted to engineering units, and merged into a single file with constant sample rate.

Maneuvers or Programmed Test Inputs

Maneuvers for stability and control data have been carefully developed to provide the maximum amount of information. It is important in this testing to excite the motions that affect the derivatives in question to make them identifiable from the flight data. Because of the limited testing of the Space Shuttle and the characteristics of the flight control system, precise maneuver design and execution are very important.

The flight control system of the Space Shuttle Orbiter heavily modifies inputs through the stick and is designed to damp oscillations and transients. This design causes difficulty in pulsing a control surface. In pulsing the Orbiter, the control system modifies the stick input with filters, responds to rate and acceleration feedback values, and damps the response with further surface

motion. In general when the vehicle is pulsed, all available controls are put into action to quickly damp the vehicle motion. Such control system implementation can cause difficulty in separating the effects of various control and response variables.

Programmed test inputs were developed to somewhat overcome this important problem and to provide exact designed inputs. This type of maneuver is input directly to the flight control system through onboard software. The amplitude and timing are governed by programmed variables to generate a specific input at a predesignated flight condition.

These programmed inputs are made through the flight control system, and they go to an integrator at the point where the surface deflection is commanded. The input is added to the command, a surface rate, which is then processed through a maximum rate-limit function. Signals can be sent to the elevon, aileron, and rudder as well as to the pitch, roll, and yaw jets. The input from the automatic PTI is not completely free of flight control system interference, but the design does allow for enhanced maneuvers.

All of the stability and control flight data discussed in the remainder of this paper were obtained from PTI maneuvers. Very small maneuvers, an order of magnitude smaller than those from the PTI, were successfully analyzed for the Orbiter, and those results are discussed in detail in references 6 and 7.

Maximum Likelihood, or Extraction, Method

The aircraft equations of motion can be written as a general system model in the continuous discrete form as follows:

$$\mathbf{x}(t_0) = \mathbf{x}_0 \quad (1)$$

$$\dot{\mathbf{x}}(t) = f[\mathbf{x}(t), \mathbf{u}(t), \boldsymbol{\xi}] + \mathbf{F}(\boldsymbol{\xi})\mathbf{n}(t) \quad (2)$$

$$\mathbf{z}(t_i) = g[\mathbf{x}(t_i), \mathbf{u}(t_i), \boldsymbol{\xi}] + \mathbf{G}(\boldsymbol{\xi})\boldsymbol{\eta}_i \quad (3)$$

where \mathbf{x} is the state vector, \mathbf{z} is the observation vector, f and g are system state and observation functions, \mathbf{u} is the known control input vector, $\boldsymbol{\xi}$ is the vector of unknown parameters, \mathbf{n} is the state noise vector, $\boldsymbol{\eta}$ is the measurement noise vector, \mathbf{F} and \mathbf{G} are system matrices, and t is time. The state noise vector, \mathbf{n} , is assumed to be zero-mean white Gaussian and stationary, and the measurement noise vector, $\boldsymbol{\eta}$, is assumed to be a sequence of independent Gaussian random variables with zero-mean and identity covariance. For each possible estimate of the unknown parameters, a probability that the aircraft response time histories will attain values near the observed values can then be defined. The maximum likelihood estimates are defined as those that maximize this probability. Maximum likelihood estimation has many desirable statistical characteristics; for example, it yields asymptotically unbiased, consistent, and efficient estimates (ref. 8).

If there is no state noise, then the maximum likelihood estimator minimizes the cost function

$$J(\xi) = \frac{1}{2} \sum_{i=1}^N [\mathbf{z}(t_i) - \tilde{\mathbf{z}}_{\xi}(t_i)]^* (\mathbf{G}\mathbf{G}^*)^{-1} [\mathbf{z}(t_i) - \tilde{\mathbf{z}}_{\xi}(t_i)] + \frac{1}{2} N \ln |(\mathbf{G}\mathbf{G}^*)| \quad (4)$$

where $\mathbf{G}\mathbf{G}^*$ is the measurement noise covariance matrix, $\tilde{\mathbf{z}}_{\xi}(t_i)$ is the predicted response estimate of \mathbf{z} at t_i for a given value of the unknown parameter vector ξ , and N is the number of time points. The cost function is a function of the differences between the measured and computed time histories.

If equations (2) and (3) are linearized (as is the case for the stability and control derivatives in the aircraft problem), then

$$\mathbf{x}(t_0) = \mathbf{x}_0 \quad (5)$$

$$\dot{\mathbf{x}}(t) = \mathbf{A}\mathbf{x}(t) + \mathbf{B}\mathbf{u}(t) + \mathbf{F}\mathbf{n}(t) \quad (6)$$

$$\mathbf{z}(t_i) = \mathbf{C}\mathbf{x}(t_i) + \mathbf{D}\mathbf{u}(t_i) + \mathbf{G}\eta_i \quad (7)$$

where \mathbf{A} , \mathbf{B} , \mathbf{C} , and \mathbf{D} are system matrices. For the no-state-noise case, the $\tilde{\mathbf{z}}_{\xi}(t_i)$ term of equation (4) can be approximated by

$$\tilde{\mathbf{x}}_{\xi}(t_0) = \mathbf{x}_0(\xi) \quad (8)$$

$$\tilde{\mathbf{x}}_{\xi}(t_{i+1}) = \phi \tilde{\mathbf{x}}_{\xi}(t_i) + \psi [\mathbf{u}(t_i) - \mathbf{u}(t_{i+1})]/2 \quad (9)$$

$$\tilde{\mathbf{z}}_{\xi}(t_i) = \mathbf{C}\tilde{\mathbf{x}}_{\xi}(t_i) + \mathbf{D}\mathbf{u}(t_i) \quad (10)$$

where the transition matrix, ϕ , and the integral of the transition matrix, ψ , are given by

$$\phi = \exp [\mathbf{A}(t_{i+1} - t_i)] \quad (11)$$

$$\psi = \int_{t_i}^{t_{i+1}} \exp(\mathbf{A}\tau) d\tau \mathbf{B} \quad (12)$$

The Newton-Raphson algorithm (or some other minimization technique), can be applied to minimize the cost function, $J(\xi)$. Such techniques choose successive estimates of the vector of unknown coefficients, $\hat{\xi}$ (denoting estimate). If L is the iteration number, then the $L + 1$ estimate of ξ is obtained from the L estimate as

$$\hat{\xi}_{L+1} = \hat{\xi}_L - [\nabla_{\xi}^2 J(\hat{\xi}_L)]^{-1} [\nabla_{\xi}^* J(\hat{\xi}_L)] \quad (13)$$

If $(\mathbf{G}\mathbf{G}^*)^{-1}$ is assumed fixed, then the first and second gradients are defined as follows:

$$\nabla_{\xi} J(\xi) = - \sum_{i=1}^N [\mathbf{z}(t_i) - \tilde{\mathbf{z}}_{\xi}(t_i)]^* (\mathbf{G}\mathbf{G}^*)^{-1} [\nabla_{\xi} \tilde{\mathbf{z}}_{\xi}(t_i)] \quad (14)$$

$$\begin{aligned} \nabla_{\xi}^2 J(\xi) = & \sum_{i=1}^N [\nabla_{\xi} \tilde{\mathbf{z}}_{\xi}(t_i)]^* (\mathbf{G}\mathbf{G}^*)^{-1} [\nabla_{\xi} \tilde{\mathbf{z}}_{\xi}(t_i)] \\ & - \sum_{i=1}^N [\mathbf{z}(t_i) - \tilde{\mathbf{z}}_{\xi}(t_i)]^* (\mathbf{G}\mathbf{G}^*)^{-1} [\nabla_{\xi}^2 \tilde{\mathbf{z}}_{\xi}(t_i)] \end{aligned} \quad (15)$$

The Gauss-Newton approximation to the second gradient is

$$\nabla_{\xi}^2 J(\xi) \cong \sum_{i=1}^N [\nabla_{\xi} \tilde{\mathbf{z}}_{\xi}(t_i)]^* (\mathbf{G}\mathbf{G}^*)^{-1} [\nabla_{\xi} \tilde{\mathbf{z}}_{\xi}(t_i)] \quad (16)$$

The Gauss-Newton approximation is computationally much easier than the Newton-Raphson method because the second gradient of the innovation never needs to be calculated. In addition, it can have the advantage of speeding the convergence of the algorithm (ref. 4).

Figure 9 illustrates the maximum likelihood estimation concept. The measured response is compared with the estimated response, and the difference between these responses is called the response error. The cost function of equation (4) includes this response error. The minimization algorithm is used to find the coefficient values which minimize the cost function. Each iteration of this algorithm provides a new estimate of the unknown coefficients on the basis of the response error. These new estimates are then used to update values of the coefficients of the mathematical model, providing a new estimated response and, therefore, a new response error. Updating of the mathematical model continues iteratively until a convergence criterion is satisfied. The estimates resulting from this procedure are the maximum likelihood estimates.

The maximum likelihood estimator also provides a measure of the reliability of each estimate based on the information obtained from each dynamic maneuver. This measure of the reliability, analogous to the standard deviation, is called the Cramér-Rao bound (refs. 9 and 10) or the uncertainty level. The Cramér-Rao bound, as computed by current programs, should generally be used as a measure of relative rather than absolute accuracy. The bound is obtained from the approximation to the information matrix, \mathbf{H} , which is based on equation (16); the actual information matrix is defined when evaluated at the correct values (not the maximum likelihood estimates) of all the coefficients. The bound for each unknown is the square root of the corresponding diagonal element of \mathbf{H}^{-1} ; that is, for the i th unknown, the Cramér-Rao bound is $\sqrt{(\mathbf{H}^{-1})_{i,i}}$.

STABILITY AND CONTROL DERIVATIVE EXTRACTION JUSTIFICATION

There was a well-defined requirement for the extraction of stability and control derivatives from flight data for the Space Shuttle. This requirement had two sources: the need to improve the preflight predictions of the stability and control derivatives and the need to reduce the associated uncertainties of each derivative. These preflight predictions and their associated uncertainties

(ref. 1), were used for control system design, for operational envelope definition, and for high-fidelity flight-training simulators. These flight data were required to update the coefficients of the mathematical model, so the flight control system could be improved, the operational envelope expanded, and the simulators would have increased fidelity.

Stability and control derivatives are usually determined in a flight program by performing repeated stability and control maneuvers throughout a matrix of conditions in the flight envelope of the aircraft. The coefficients and, sometimes, the form of the mathematical model originally based on preflight ground predictions are then updated with the new information. This procedure is usually followed whether the derivative extraction is done to improve the operational envelope or to obtain flight research data.

For a variety of reasons, the Space Shuttle Orbiter could not fly repeated maneuvers throughout its envelope. This limitation meant that there was not enough data to update the preflight aerodynamic data book in the traditional manner. The following discussion of the process used for the Orbiter was selectively excerpted from reference 11, which was written from the perspective of the Space Shuttle team in 1983, following the first four flights:

Stability and control testing of the Space Shuttle is driven by conflicting program desires, while limited by unique problems. Space Shuttle flights are very costly when compared with test flights of other aircraft. There is an intense desire within the program to bring the Shuttle to an operational mode. . . . On the other hand, it is important to assure the safety of entry flight and to identify the real limitations of the Shuttle through flight testing. This conflict in goals has resulted in the need for a minimum amount of highly productive testing.

Conventional flight test techniques and computer programs have formed the basis for the Shuttle flight test program. Modifications to these techniques have been necessary, however, due to the inherent constraints in Shuttle testing. Measures have been taken to ensure the quality of maneuvers and the data from them, so that the number of repeat maneuvers can be minimized.

The flight test plan developed for the Shuttle contains very few test points when compared to test programs of military aircraft. Enough maneuvers are scheduled only to verify the safety of the Shuttle entry, not enough to build a flight test data base. Where significant differences exist between the flight data and the wind-tunnel data base, further test points are scheduled [ref. 1]. . . .

Derivative [flight assessment] deltas calculated between flight and values from the Shuttle Aerodynamic Design Data Book [ref. 1] are provided to Shuttle simulators to demonstrate the safety of further testing on upcoming flights and to assure the safety of flying c.g.'s associated with planned payloads [ref. 1]. . . .

Aerodynamic test requirements have arisen from two sources. The original source is the preflight wind tunnel and the associated uncertainties. The other source of requirements is the flight data from the initial flights, during which anomalies occurred. The types of problems identified involve either potentially excessive RCS fuel usage for longitudinal and lateral trim, or potential loss of control. . . .

Preflight wind-tunnel data for the orbiter is [sic] very extensive and provided sufficient confidence to fly the initial missions under benign conditions and within a limited range of [center of gravity positions]. From wind-tunnel test data, a preflight data base was developed for use in simulators and for design of the entry guidance and flight control systems.

Uncertainties on these data were developed because of wind tunnel to flight differences noted

in previous flight test programs on other aircraft. Uncertainties were also assessed for high Mach number, low dynamic pressure flight regimes where wind tunnels were heretofore either unverified or not capable of reproducing flight conditions.

Design specifications require[d] that the orbiter be able to fly safely with a c.g. range of 65 to 67.5% of the reference body length. Extremes of this range result in the limits of trim capability necessary to operate the vehicle. At the c.g. extremes, analysis indicates combinations of the uncertainties in pitching moment and the stability and control derivatives result in potential control problems. The problem areas defined from preflight data were the drivers in setting entry flight placards. . . .

Anomalies in the actual flight data have extended the test requirements as originally conceived. These anomalies have in some cases accentuated the need for certain data already planned for. Others have pointed to a need for more concentrated investigation of certain flight regimes. . . .

These anomalies have not restricted the flight placards further. However, they have accentuated the need for data in certain flight regimes. They have also caused the planning of further testing in specific areas. . . .

The Shuttle test program is the product of significant planning and integration with other program requirements. The flight test requirements from wind-tunnel uncertainties and flight anomalies dictated the flight conditions at which maneuvers would be done. Sufficient maneuvers were planned at nominal conditions to indicate repeatability of results. Additional maneuvers were planned over the ranges of elevon and angle of attack that will be seen operationally to check coefficient sensitivities to these parameters. The test plan has been modified to provide additional information in areas where anomalies have occurred. This is necessary to establish an understanding of the anomaly and to develop a database for simulators, in areas where the wind tunnel data is deficient. . . .

The flight testing has been planned to meet program objectives. The first and most important is to open the c.g. placards as quickly as possible, to verify the safety of flying planned payloads. In addition, data resulting from tests is [sic] scheduled to support planned flight control system changes, which will improve control where in-flight aerodynamic anomalies have occurred. . . .

An important product of the flight test program is the confidence that is gained from flight test results in assessing the safety of upcoming flights. Vehicle c.g.'s associated with specific payloads must be shown to be safe. In addition, further testing in the flight test program depends on values of derivatives obtained from previous tests. For instance, it is important to understand as much as possible about stability and control characteristics for down elevon positions, before it is safe to fly with elevons at more negative settings. To accomplish this, fairings are developed for the flight test results and are provided to the Shuttle flight control system community. These fairings of "assessment" values are incorporated into simulators which are used to verify the safety of upcoming flights. Exact maneuvers and trajectory profiles are simulated with correct c.g.'s. In addition, stability analyses are performed using the flight derived aerodynamic data to update c.g. placards for the vehicle. . . .

The primary goal of the entire data extraction effort is to open c.g. placards for the Shuttle, so that the full payload carrying capability can be utilized. Through the planned maneuvers, and elevon and angle-of-attack schedules, sufficient data is [sic] to be obtained to verify the Shuttle operational safety during entry. The operational limits for c.g. have been specified to be from 65 to 67.5 percent of the reference body length.

STABILITY AND CONTROL DERIVATIVE ASSESSMENT PROCESS

This section discusses the first author's perception of the stability and control assessment process. This perception is based on experience gained while serving continuously on various Space Shuttle aerodynamics and flight test panels for the past 18 yr.

Most of the stability and controls maneuvers from the Space Shuttle flights were analyzed by four sets of analysts. These four sets were composed of groups at the Rockwell International Space Division (Rockwell), Downey, California, the NASA Johnson Space Center (JSC), Houston, Texas, the Air Force Flight Test Center (AFFTC), Edwards Air Force Base, California, and the NASA Dryden Flight Research Facility (NASA-Dryden), Edwards, California. All four sets of analysts used the maximum likelihood estimation algorithm (MMLE) derivative extraction computer program (ref. 12). This discussion is based on the MMLE analysis of the Space Shuttle Orbiter PTI maneuvers by these four sets of analysts. Some of this work was previously reported in references 11, 13, and 14. Many other Orbiter maneuvers, including bank angle reversals and incidental vehicle motions, were analyzed. Although not presented in this paper, results of these analyses were used to resolve ambiguous information obtained from the PTI maneuvers.

The flight data used to improve the original preflight aerodynamic data book predictions and the associated uncertainties (ref. 1) were originally viewed as providing incremental changes to the data book. These incremental changes were called flight assessment deltas (FAD's). The delta in this name refers to the incremental change. The FAD's were generated after STS-2, -4, -6, -9, -14, and -26.

The AFFTC stopped analyzing these data after the first 13 flights. An additional change in the aerodynamic data book is due after STS-57. The PTI's have been analyzed by the three remaining groups through the 54 Space Shuttle flights (through STS-56). At this time, the Space Shuttle has flown 54 flights: 13 by *Columbia*, 10 by *Challenger*, 16 by *Discovery*, 12 by *Atlantis*, and 3 by *Endeavour*. Dynamic maneuvers from 45 of these have been analyzed. Data from these flights have been analyzed, and the results are still being assessed for incorporation into the aerodynamic data book in the fall of 1993. The results of this latest assessment are not included in this paper.

As discussed in the Stability and Control Derivative Extraction Justification section, one of the primary reasons that the stability and control derivatives are determined is to expand the c.g. envelope. The current longitudinal c.g. envelope is from 1076.7 in. (65-percent reference body length) to 1109.0 in. (67.5-percent reference body length). Figure 10 shows the current longitudinal and lateral c.g. envelope, and all centers of gravity flown are shown.

The remainder of this paper concentrates on the results of the analyses that were incorporated into the preflight aerodynamic data book from STS-1 through STS-26. This set of incremental changes is known as FAD-26. Rockwell was charged with implementing the procedure for defining FAD's. Briefly, this implementation involved collecting the estimated stability and control derivatives from the four groups of analysts and presenting these estimated derivatives in various formats, so a consensus fairing for the derivatives and the associated uncertainties could be assessed by the four groups of analysts and by other aerodynamics experts.

The four primary sets of Space Shuttle Orbiter flight condition parameters are Mach number, angle of attack, elevon position, and body flap position. At high altitudes and low dynamic pressures (below 20 lb/ft²), dynamic pressure was also used as a primary parameter. Mass flow

ratio and momentum ratio for the RCS jets were also examined (ref. 13). Because Mach number decreases monotonically for the Orbiter during entry, most of the stability and control derivatives estimated from flight were assessed primarily as functions of true (not GPC-derived) Mach number.

Rockwell plotted the stability and control derivatives as functions of two flight condition parameters, using carpet plots to aid in assessing which were the primary variables that affected given derivatives. In addition, Rockwell provided data comparing the flight-derived estimates with the aerodynamic data book predictions. This effort included procedures and recommendations for merging the FAD's with the aerodynamic data book values for regions where no flight data were provided. The aerodynamic data book predictions used in these comparisons were obtained by interpolating all of the primary flight condition parameters (for example, Mach number, angle of attack, center of gravity location, altitude, and elevon and body flap positions) so that the flight-derived estimates were compared with the predictions at the same flight conditions.

DERIVATIVE RESULTS

In this section, the stability and control derivative estimates obtained from the flight are compared with predictions. Complicated functional dependence of the derivatives predicted in reference 1 cannot be validated by the data from a single flight. These predictions are a function of many parameters defining the flight conditions. Such parameters include Mach number, angle of attack, altitude, dynamic pressure, body flap position, and elevon deflection. Between entry interface (400,000 ft) and final approach, the true Mach number monotonically decreased from above 28 to below 1. Thus, for any particular Mach number in any given flight, these data are available only at a single value of angle of attack, dynamic pressure, altitude, body flap position, and other parameters.

Several of these parameters continually change; therefore, conclusively attributing any trends observed in the derivatives of specific flight condition parameters to a given factor is impossible. Most of the estimates presented here are plotted as a function of true Mach number. This form of presentation is adopted only for convenience and is not meant to imply that the trends observed are necessarily directly related to Mach number. For instance, the trends between Mach 12 and 2 may be more influenced by the angle of attack, which decreases from 40° to 10°, than by the Mach number. The predictions were determined at the particular flight condition which occurred at each Mach number of the flight. Thus, these predictions are comparable to the flight results.

Figure 11 shows elevon deflection, body flap deflection, and angle of attack as functions of Mach number for Space Shuttle Orbiter flights from STS-1 through STS-26. This figure shows why a large amount of scatter exists in the plots of the derivatives as functions of Mach number. Using the Mach number obscures the large changes in flight condition, and much of the scatter is attributable to these large changes in flight conditions. In reality, these derivatives were plotted against each other in a carpet plot fashion. To define the flight fairing, this approach was used to account, as much as possible, for variations in flight condition parameters. In a normal flight research program, a matrix of flight conditions (Mach number, angle of attack, elevon position, and body flap position) would be specified and maneuvers performed at each combination of conditions. In this manner, the effect of each flight condition parameter can be assessed independently of the other flight condition parameters. For the Orbiter, these maneuvers are included in the reentry to reduce the uncertainties of the estimates, rather than being used for research purposes to determine

which parameters have given effects. Therefore, the matrix of flight conditions for the Orbiter is too sparse for full cross plotting. This inability to cross-plot because of sparseness results in a significant amount of scatter, as seen in the derivative plots.

The effects of the rotary derivatives are very small for the high-speed flight regimes. Primarily for this reason, all of the maneuvers were analyzed with the rotary derivatives set at the predicted nominal values from reference 1. Therefore at Mach numbers below 3, where the rotary derivatives begin to have some effect, any errors in the predicted rotary derivatives affect the estimates of other derivatives. The effect would appear primarily in the control derivative estimates because changes in these derivatives would best account for errors in the rotary derivatives. The effect would be unnoticeable above a Mach number of 3. The RCS yaw jet derivatives were determined throughout the entry, offering a significant set of flight data on RCS jet interference effects. The RCS pitch and roll jets were active only during the early portions of the entry. Again, note that dynamic pressure, altitude, velocity, and angles of attack and sideslip are GPC parameters from the inertial measurement unit. Errors in these parameters will result in errors in the estimated stability and control derivatives. Below Mach 2, buffet, which degrades the accuracy of the derivative estimates, was encountered.

The moments and forces due to yaw jets are so instantaneous and so large that they have a masking effect on the aerodynamic control derivatives. Better estimates of the aerodynamic control derivatives could be obtained if the RCS jets could be held to zero during the aerodynamic control surface pulse portion of the maneuver.

In addition to the potential causes of data scatter peculiar to the Space Shuttle Orbiter, reasons for error or scatter also occur in the analysis of flight data. These reasons include (1) accuracy of vehicle mass properties (mass, center-of-gravity location, and moments of inertia); (2) accuracy of instrumentation system (calibration, location, and orientation errors); (3) accuracy in data recording (data resolution, sample rate effects, and time skews); (4) accuracy of sensors (sensor error and noise); (5) size of maneuver; (6) excitation of state variables; (7) errors in mathematical models; and (8) independence of state and control variables. Some of these general errors are discussed in more detail in references 4 and 15.

A standard format is followed in figures 12 through 26. The derivatives are plotted as a function of true Mach number in the upper portion of the figures. The value of an estimate itself is represented by a symbol, and the uncertainty level (refs. 15 and 16) is represented by a vertical bar. (The larger the uncertainty level, the less reliable the estimate.) The uncertainty level is 10 times the calculated Cramér-Rao bound. A value of 10 was chosen because there was not a great deal of data, and the maneuvers were not ideal for derivative estimation. The dotted fairing on each plot represents the nominal predictions from the preflight aerodynamic data book. The solid line on each plot is the fairing of the flight-determined derivatives based on the estimates of all four groups of analysts. The lower part of the figure shows the delta values, which are the flight data value minus the flight-fairing value at that condition, plotted against true Mach number. The dashed lines (on the lower part) represent the current uncertainty bounds based on flight and prediction results.

Results of Analyses at NASA-Dryden

The stability and control derivative estimates from Space Shuttle flights STS-1 through STS-26 are presented in this subsection. For purposes of discussion, it is easiest to examine the results obtained from just one group of analysts. This approach eliminates the scatter which results from the differing estimates by various groups. In addition, use of fewer data points makes it easier to see the uncertainty level for each estimate. The flight fairing, solid line shown on the figures 12 through 23, is the fairing based on the estimates of all four groups of analysts. The key NASA-Dryden results are discussed in the following sub-subsections. Then, some key results from the four groups of analysts are discussed in the Results of Analyses by All Groups subsection.

Lateral-Directional Stability and Control Derivative Estimates

Figure 12 shows the directional stability, C_{n_β} , estimated by NASA-Dryden for flights STS-1 through STS-26. In the upper part of figure 12(a), as in all figures discussed in this and the Longitudinal Results sub-subsection, the dotted line is the fairing from the preflight aerodynamic data book (ref. 1), and the solid line is the fairing based on the flight-derived estimates from all the analyst groups. Each symbol is the NASA-Dryden estimate for the PTI maneuver, and the vertical bar is the uncertainty level of the estimate for that maneuver. Estimates with small uncertainty levels are considered to be better estimates than those with large uncertainty levels. The differences between the fairing for the estimates from all groups (solid line) and the NASA-Dryden estimates are shown in the lower part of figure 12(a) as δC_{n_β} ; that is, for δC_{n_β} ,

$$\delta C_{n_\beta} = C_{n_\beta \text{ flight estimate}} - (C_{n_\beta \text{ data book}} + C_{n_\beta \text{ FAD}}) \quad (17)$$

The dashed lines in the lower part of figure 12(a) show the flight-derived uncertainties of the derivatives. For these uncertainties to be meaningful, most of the data points should lie between the dashed lines. In particular, the data points with the small vertical bounds should be within the dashed lines.

Figure 12(b) shows only the results for Mach numbers less than 7. Showing just these estimates makes the individual estimates more clearly visible. Although the scatter in the estimates is fairly large (as discussed in the Derivative Results section), the trends indicated by the flight fairing can be clearly seen, and most of the estimates are between the flight-derived uncertainties.

Before discussing other derivatives, it may be useful to examine the reasons for some of the scatter in the estimates. The effect of the scatter for Mach number is shown in figure 12(b), for elevon position in figure 12(c), and for angle of attack in figure 12(d). Fourteen estimates for Mach numbers between 4 and 5 are plotted as a function of elevon position in figure 12(c) and as a function of angle of attack in figure 12(d). The individual points can now be located on figures 12(b), (c), and (d), and the effects of the three flight condition parameters can be examined. In addition, effects of the flight estimates and the corresponding predictions can be seen for each of these three parameters. Much of the scatter results from change in the flight condition parameter and not from randomness in the estimate.

The significant differences between flight and prediction occur between Mach 1 and 3, between Mach 5 and 6 (fig. 12(b)), and above Mach 20 (fig. 12(a)). Adjusting the flight simulator to match

the flight-derived values resulted in improved harmony between the flight simulator and the vehicle, which was the primary purpose of analyzing the PTI maneuvers.

Figure 13 shows the dihedral effect, C_{l_β} , as a function of Mach number. As desired, most of the estimates of δC_{l_β} fall between the dashed lines in the lower part of figure 13. Cross-plotting C_{l_β} as a function of elevon position and angle of attack yields results similar to those for C_{n_β} . (These plots are not shown here.) The most significant difference between flight and prediction is that the flight values show a 40- to 50-percent reduction in the magnitude of C_{l_β} for Mach numbers above 15.

Figure 14 shows the comparison of flight and prediction for roll control power, $C_{l_{\delta a}}$. Once again, the estimates of $\delta C_{l_{\delta a}}$ fall between the dashed lines in the lower part of figure 14(a). A 10- to 20-percent reduction occurred for flight to prediction between Mach 5 and 13 and between Mach 18 and 22. The reduction in effectiveness between Mach 18 and 22 is actually an effect of elevon position, which can be seen in figure 14(b). The reduced effectiveness is a result of the effect of up elevon position between 2° and 4°.

Figure 15 shows the coefficient of side force due to two yaw jets, $C_{Y_{YJ_2}}$, as a function of mass flow ratio, \dot{M}_J/\dot{M}_∞ . The importance of the yaw jets was discussed in the Orbiter Stability and Control Example section and is also discussed extensively in references 13 and 17. Good agreement exists between flight and prediction for this derivative. The importance of considering the uncertainty levels is illustrated by the large scatter of those estimates with large uncertainty levels. Most of the $\delta C_{Y_{YJ_2}}$ points lying outside the dashed line in the lower part of the figure have large uncertainty levels.

Figure 16 shows the coefficient of rolling moment due to two yaw jets, $C_{l_{YJ_2}}$, as a function of mass flow ratio, \dot{M}_J/\dot{M}_∞ . The large difference between flight and prediction at high mass flow ratios is the same effect shown for L_{YJ} at high Mach numbers in the Orbiter Stability and Control Example section in figure 6. After the flight fairing is subtracted from the estimates, all of the resulting $\delta C_{l_{YJ_2}}$ values fall between the dashed uncertainty bounds on the lower part of the figure.

Figure 17 shows the effect of four yaw jets firing on the rolling moment, $C_{l_{YJ_4}}$, plotted as a function of mass flow ratio, \dot{M}_J/\dot{M}_∞ . The discrepancy between flight and prediction at high mass flow ratios is significant but not as large as the discrepancy for two yaw jets firing (fig. 16). The resulting $\delta C_{l_{YJ_4}}$ values lie well within the flight-derived uncertainties. The lower flight estimates of $C_{l_{YJ_4}}$ at values of \dot{M}_J/\dot{M}_∞ between 0.002 and 0.001 (corresponding to a Mach number between 5 and 10) were not seen for $C_{l_{YJ_2}}$. The difference between the effect on rolling moment of two and four yaw jets ($C_{l_{YJ_2}}$ and $C_{l_{YJ_4}}$) was not predicted. As a result, this effect and a similar effect on C_Y and C_n for yaw jet firings had to be added to the Orbiter mathematical model. This new parameter can be defined in the same manner as the rest of the FAD, but this effect was one of several found in flight that was best implemented as changes in the form of the mathematical model of the Orbiter rather than as an incremental change in just the values of the stability and control derivatives.

Figure 18 shows the coefficient of rolling moment due to roll jets, $C_{l_{RJ}}$, as a function of the jet momentum ratio, ϕ_J/ϕ_∞ . The change in the values of the jet momentum ratio is small because the roll jets only operate at dynamic pressures below 10 lb/ft². The faired flight value of $C_{l_{RJ}}$ is essentially double that of the prediction.

Longitudinal Results

This sub-subsection discusses the results of the NASA-Dryden analysis for the longitudinal PTI maneuvers. Figure 19 shows the longitudinal stability term, C_{m_α} , as a function of Mach number. The flight data confirm the prediction throughout most of the range. Most of the δC_{m_α} values with small uncertainties are between the dashed lines on the lower part of this figure. A disappointingly large amount of scatter exists for this important and usually easily extracted parameter. Some of the scatter was caused by the effects of the other flight condition parameters. However, still more scatter exists than would normally occur. A major cause of the unusually high scatter is the extremely low sample rate of 1 sample/sec for angle of attack. (See the list of instrumentation properties in the Flight Data Measurements subsection.) The effect of the low sample rate is compounded by the associated unknown sample lags and the rolling time skews. Until higher sample rate data are obtained, the estimates of C_{m_α} will not improve (ref. 7).

Figures 20 and 21 show the coefficients of pitching moment due to elevon position, δ_e , and elevon position squared, δ_e^2 , respectively, or $C_{m_{\delta_{e0}}}$ and $C_{m_{\delta_e^2}}$. The original model included only $C_{m_{\delta_e}}$ effects because $C_{m_{\delta_e^2}}$ effects were assumed to be negligible. These maneuvers could not be successfully analyzed with only the $C_{m_{\delta_e}}$ term, so $C_{m_{\delta_e^2}}$ was added. Then, the results of the analysis with the added $C_{m_{\delta_e^2}}$ term compared favorably with the original predictions (ref. 7). Figures 20 and 21 show the flight-derived values of $C_{m_{\delta_{e0}}}$ and $C_{m_{\delta_e^2}}$; however, because of the original assumptions, there are no predictions for $C_{m_{\delta_e^2}}$ on figure 21(a). To check this effect on the predicted model, the nonlinear curve, $C_{m_{\delta_{e0}}} \delta_e + C_{m_{\delta_e^2}} \delta_e^2$ (determined from flight), must be compared with the aerodynamic data book values. This comparison was made. The flight values were consistent with prediction; therefore, no FAD update was needed for C_m due to δ_e .

Figure 22 shows the pitching moment due to two yaw jets firing, $C_{m_{YJ_2}}$, as a function of mass flow ratio, \dot{M}_J/\dot{M}_∞ . The flight value is lower than the prediction above \dot{M}_J/\dot{M}_∞ of 0.0005. The flight values are essentially zero at mass flow ratios below 0.01.

Figure 23 shows the coefficient of pitching moment due to down-firing jets, $C_{m_{DJ}}$, as a function of momentum ratio, ϕ_J/ϕ_∞ . The values found throughout the range of momentum ratios tested were 50 percent more negative than those predicted. The down-firing jets operate only below a dynamic pressure of 40 lb/ft². All of the points with small uncertainty for two down-firing jets firing occur within the uncertainty bounds for $\delta C_{m_{DJ}}$. This result shows, once again, the value of considering the uncertainty level when assessing the flight-derived values.

Results of Analyses by All Groups

This subsection describes the results of analyses by all four groups. Because results from all four groups of analysts were included, the number of points increased greatly, and the uncertainty levels (the vertical bars in figures 12 through 23) are not included on the figures. Some of the results presented here were also presented in the Results of Analyses at NASA-Dryden subsection.

Programmed Test Input Estimates

Only the three derivatives presented in figures 24, 25, and 26 are discussed in this sub-subsection. In the cases of the other derivatives discussed in the Results of Analyses at NASA-Dryden subsection, similar results were obtained by the four analyst groups.

Figure 24 shows C_{n_β} as a function of Mach number for all the PTI maneuvers as determined by the four sets of analysts. These flight and prediction fairings are the same as those used in figure 12(a). The same analysis and cross plotting were used to assess the contributions of Mach number, elevon position, angle of attack, and body flap position to the estimates of C_{n_β} . As can be seen in the lower part of figure 24, most points fall inside the uncertainty bounds. Flight-derived C_{n_β} estimates were used to formulate FAD-26. This use improved the fidelity between the flight data and the simulator. The reduction of uncertainty shown in FAD-26 allowed an expanded Space Shuttle Orbiter flight envelope.

Figure 25 shows the variation of $C_{l_{\delta_a}}$ with Mach number and elevon position, δ_e . The estimates from all groups of analysts cluster fairly well near those estimated by NASA-Dryden (fig. 14). This clustering shows how strongly this derivative is defined by the PTI maneuvers. The strong dependence of $C_{l_{\delta_a}}$ on elevon position is, once again, shown in figure 25(b). Few of the estimates fall outside the uncertainty bounds for this derivative, which reduced the overall uncertainty for this extremely important control derivative. This reduction in uncertainty improved the overall robustness of the Orbiter control system.

Figure 26 shows the results from all of the analyst groups for $C_{l_{YJ_2}}$ as a function of mass flow ratio, \dot{M}_J/\dot{M}_∞ . The same strong trend is shown here, at high mass flow ratios, as was seen in the NASA-Dryden analysis (fig. 16). As shown in the lower half of the figure, virtually all of the data from all the analyst groups fall between the uncertainty bounds at the high mass flow ratios. These results indicate the preponderance of evidence that reduced the uncertainty in $C_{l_{YJ_2}}$.

Flight Assessment Deltas-Only Results

Figure 27 presents the remainder of the flight assessment deltas which were changed between FAD-14 and FAD-26 and which have not been previously discussed. The differences (or deltas) discussed here, such as ΔC_{Y_β} (fig. 27(a)), are the increments added to the preflight aerodynamic data book values to get the current best representation of the flight-derived stability and control derivatives. These data are presented as a function of the Mach number, mass flow ratio, or momentum ratio. These data are taken from reference 18. These figures show that the flight analyses have resulted in significant changes from the original predictions for many of the derivatives and their associated uncertainties. In addition, these changes continued to be made well into the flight program, as more flight data were obtained after FAD-14, between STS-14 and STS-26. The changes most significant to the Space Shuttle Orbiter envelope expansion (and not discussed before) were the changes in $C_{n_{\delta_a}}$, $C_{n_{\delta_r}}$, $C_{l_{\delta_r}}$, and $C_{m_{BF}}$. Results of the FAD for these parameters (and all parameters discussed previously) have resulted in improved harmony between the flight simulation and the flight vehicle.

To assess the effectiveness of the determination of the stability and control derivatives from the Orbiter flight data, it is instructive to examine the case of an important derivative, looking at the

changes in the derivative as a function of the FAD number. Such a derivative is directional stability, $C_{n\beta}$, for which $\Delta C_{n\beta}$ from a number of FAD's is plotted against Mach number (fig. 28). The $\Delta C_{n\beta}$ fairing for FAD-2 was positive from Mach 1 to Mach 3, negative from Mach 3 to Mach 7, positive from Mach 7 to Mach 13, and negative (and small) above Mach 13. Each succeeding FAD showed the same general pattern of positive and negative increments. However, the size of the increment and the Mach number "switch points" were modified in each succeeding FAD, as increased numbers of maneuvers were analyzed. As can be seen, the refinement in the FAD's is an iterative process with each successive FAD adding more smoothness to $\Delta C_{n\beta}$. In FAD-26, $\Delta C_{n\beta}$ is a fairly smooth curve, with smaller changes in the positive and negative increments as compared with earlier versions. This refinement shows the value of having more PTI maneuvers at a wide variety of flight conditions.

Figure 29 is a final illustration of the value of the FAD for improving the estimated value of a derivative and reducing the overall uncertainty range of a derivative. The $\Delta C_{l\beta}$ is shown with its associated flight-derived uncertainty for FAD-26. The original preflight aerodynamic data book variation for $C_{l\beta}$ is also shown. It can be seen that more maneuvers improve the estimates of the derivative and reduce the flight-derived uncertainty. Although the change in the derivative is quite substantial hypersonically, particularly above Mach 16, the uncertainty in that region is reduced to 40 percent of the original, preoperational variation. The combination of the estimate improvement and the uncertainty reduction has a substantial effect on the operational envelope of the vehicle. This fact, coupled with the associated improved robustness of the control system, adds markedly to the overall safety margin of the Space Shuttle Orbiter reentry. A further discussion of related Space Shuttle issues is found in reference 19.

CENTER-OF-PRESSURE LOCATION

The STS-1 showed that significantly more body flap deflection was required to trim the vehicle hypersonically at an angle of attack of 40° than was predicted, as shown in figure 30 (ref. 14). During entry, the Space Shuttle is preprogrammed to fly at a given angle of attack for each Mach number. Because the angle of attack is maintained by setting the elevon at a position scheduled by angle of attack and Mach number, the body flap is deflected to maintain that angle of attack. To maintain 40° angle of attack hypersonically on STS-1, the body flap was deflected to 16° instead of the predicted 7° . Because 9° more body flap deflection than predicted was required, the body flap experienced more heating than predicted. The misprediction also resulted in the body flap being deflected to within 5° of its maximum deflection to trim the vehicle. In addition, increases in deflection of the body flap increase drag. This increased drag reduces the cross-range capability.

To examine this misprediction of body flap trim position, the location of the center of pressure was investigated. Figure 31 shows a comparison between flight and predicted locations of the center of pressure plotted as a function of Mach number for STS-2 (ref. 20). Variations for the prediction are also shown. These flight data were well outside of the predicted variations. Above Mach 16, the misprediction is about 0.8 percent of the body length, or 10 in. The error must be due to a misprediction of pitching moment, a misprediction of normal force, or an error in the location of the flight center of gravity. Error in the flight center-of-gravity position was less than 1 in. Also, the normal force predictions and flight values agreed fairly well; therefore, almost all of this 10-in. error was caused by a misprediction in the pitching moment. For the Space Shuttle, the

pitching moment is a function of coefficients of pitching moment due to angle of attack (C_{m_α}), pitching moment due to elevon deflection ($C_{m_{\delta_e}}$), pitching moment due to body flap deflection ($C_{m_{BF}}$), and pitching moment bias (C_{m_0}) at a given Mach number and angle of attack.

Figure 19 shows the flight-derived estimates of C_{m_α} , figure 20 shows $C_{m_{\delta_e}}$, and figure 27(q) shows $C_{m_{BF}}$ for the Space Shuttle flights through STS-26. Above Mach 16, the predictions and flight estimates agree well for these three derivatives. Thus, the error in body flap deflection required for trim is attributable to C_{m_0} . The error in C_{m_0} that would account for the discrepancy shown in figure 31 would be about 0.03 nose up. An error in C_{m_0} up to about 0.020 to 0.025 can be attributed to the real gas effects and Mach number effects. Neither effect was completely simulated in wind tunnels (refs. 21 and 22).

Between Mach 16 and 8, the center-of-pressure position misprediction went from 0.8 percent to less than 0.1 percent (fig. 31). Real gas effects become less important as the Mach number decreases. Some of the error in center-of-pressure location prediction between Mach 16 and 8 may be attributed to the misprediction in boundary-layer transition (refs. 23 and 24). Preflight predictions indicated that boundary-layer transition would start to occur at Mach 16, but the flight data indicated that the boundary layer transitions quickly at about Mach 8. This delayed transition may also affect some of the stability and control derivatives. The real gas effects, the delayed boundary-layer transition, and the rolling moment due to yaw jets ($C_{l_{YJ}}$) are the three phenomena observed in flight for the Space Shuttle Orbiter which are of most general research interest at this time.

CONCLUDING REMARKS

The goal of expanding the operational flight envelope of the Space Shuttle Orbiter was achieved, but the approach used to do so clouded some of the research value of the results. The extraction of the stability and control derivatives was justified by operational, not research, considerations. Still, the discussion in this paper shows that there have been some significant research results. However, using flight results to update the predicted database of the Orbiter is one of the most completely documented processes for any flight vehicle. Such thorough documentation processes followed from the requirement for analysis of flight data for control system updates and for expansion of the operational flight envelope.

The flight-derived stability and control derivative results described here document the outcome of this important process. These results show significant changes in many important stability and control derivatives from the preflight database. The process has also shown why the knowledge of the stability and control derivatives improves with the number of flights. The most interesting aerodynamic research results were the real gas effects which resulted in a 10-in. misprediction of the center-of-pressure location, the delay in boundary-layer transition from Mach 15 to 8, and the interference effects of the rolling moment due to the firing of the yaw jets.

REFERENCES

1. *Aerodynamic Design Data Book Orbiter Vehicle STS-1*, SD72-5H-0060 revision M, Rockwell International, Space Division, Nov. 1980.
2. Weil, Joseph and Bruce G. Powers, *Correlation of Predicted and Flight Derived Stability and Control Derivatives—With Particular Application to Tailless Delta Wing Configurations*, NASA TM-81361, July 1981.
3. Iliff, Kenneth W., "AIAA Dryden Research Lectureship—Aircraft Parameter Estimation," AIAA-87-0623, Jan. 1987.
4. Maine, Richard E. and Kenneth W. Iliff, *Application of Parameter Estimation to Aircraft Stability and Control—The Output-Error Approach*, NASA RP-1168, 1986.
5. Throckmorton, David A., "Shuttle Entry Aerothermodynamic Flight Research: The Orbiter Experiments (OEX) Program," AIAA 92-3987, July 1992.
6. Iliff, Kenneth W., Richard E. Maine, and Douglas R. Cooke, "Selected Stability and Control Derivatives From the First Space Shuttle Entry," AIAA 81-2451, Nov. 1981.
7. Maine, R.E. and K.W. Iliff, "Selected Stability and Control Derivatives From the First Three Space Shuttle Entries," AIAA 82-1318, Aug. 1982.
8. Balakrishnan, A.V., *Communication Theory*, McGraw-Hill, New York, 1968.
9. Maine, Richard E. and Kenneth W. Iliff, *Identification of Dynamic Systems*, NASA RP-1138, 1985.
10. Iliff, Kenneth W. and Richard E. Maine, "More Than You May Want To Know About Maximum Likelihood Estimation," AIAA 84-2070-CP, Aug. 1984. (See also NASA TM-85905, 1985.)
11. Cooke, Douglas R., "Minimum Testing of the Space Shuttle Orbiter for Stability and Control Derivatives," *Shuttle Performance: Lessons Learned*, NASA CP-2283, pt. 1, Mar. 1983, pp. 447-471.
12. Maine, Richard E. and Kenneth W. Iliff, *User's Manual for MMLE3, A General FORTRAN Program for Maximum Likelihood Parameter Estimation*, NASA TP-1563, 1980.
13. Stone, J.S., J.J. Baumbach, and B.B. Roberts, "Space Shuttle Orbiter Reaction Control Subsystem Flight Data Anomalies," *Shuttle Performance: Lessons Learned*, NASA CP-2283, pt. 1, Mar. 1983, pp. 381-395.
14. Kirsten, Paul W., David F. Richardson, and Charles M. Wilson, "Predicted and Flight Test Results of the Performance, Stability and Control of the Space Shuttle From Reentry to Landing," *Shuttle Performance: Lessons Learned*, NASA CP-2283, pt. 1, Mar. 1983, pp. 509-524.

15. Iliff, Kenneth W., Richard E. Maine, and T.D. Montgomery, *Important Factors in the Maximum Likelihood Analysis of Flight Test Maneuvers*, NASA TP-1459, 1979.
16. Iliff, Kenneth W., "Aircraft Identification Experience, *Parameter Identification*, AGARD-LS-104, paper 6, 29 Oct.–2 Nov. 1979.
17. Scallion, W.I. et al., "Space Shuttle Third Flight (STS-3) Entry RCS Analysis," AIAA 83-0116, Jan. 1983.
18. *Flight Assessment Package Orbiter Aerodynamics: FAD26*, NASA JSC-22078, Apr. 1986.
19. *Shuttle Performance: Lessons Learned*, NASA CP-2283, pts. 1 and 2, 1983.
20. Romere, Paul O. and A. Miles Whitnah, "Space Shuttle Entry Longitudinal Aerodynamic Comparisons of Flights 1–4 With Preflight Predictions," *Shuttle Performance: Lessons Learned*, NASA CP-2283, pt. 1, 1983, pp. 283–307.
21. Griffith, B.J., J.R. Maus, and J.T. Best, "Explanation of the Hypersonic Longitudinal Stability Problem—Lessons Learned," *Shuttle Performance: Lessons Learned*, NASA CP-2283, pt. 1, 1983, pp. 347–380.
22. Woods, W.C., J.P. Arrington, and H.H. Hamilton, II, "A Review of Preflight Estimates of Real-Gas Effects on Space Shuttle Aerodynamic Characteristics," *Shuttle Performance: Lessons Learned*, NASA CP-2283, pt. 1, 1983, pp. 309–346.
23. Iliff, Kenneth W. and Mary F. Shafer, "Space Shuttle Hypersonic Flight Research and the Comparison to Ground Test Results (Invited)," AIAA-92-3988, July 1992.
24. Harthun, M.H., C.B. Blumer, and B.A. Miller, "Orbiter Windward Surface Entry Heating: Post-Orbital Flight Test Program Update," *Shuttle Performance: Lessons Learned*, NASA CP-2283, pt. 2, 1983, pp. 781–804.

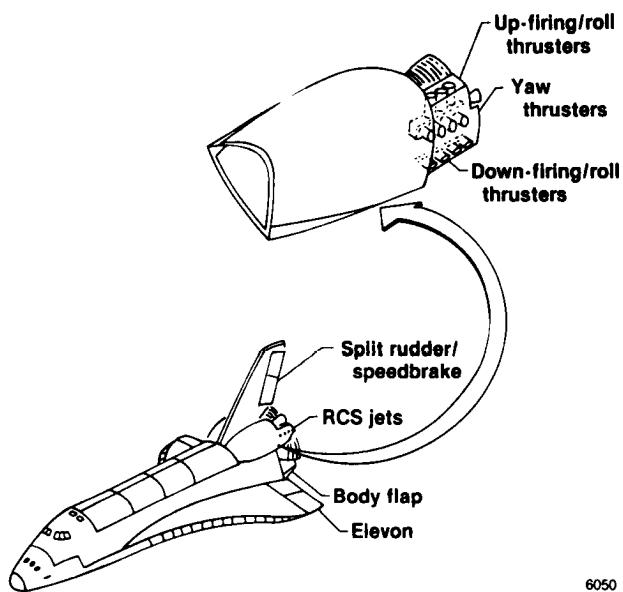


Figure 1. Space Shuttle Orbiter configuration.

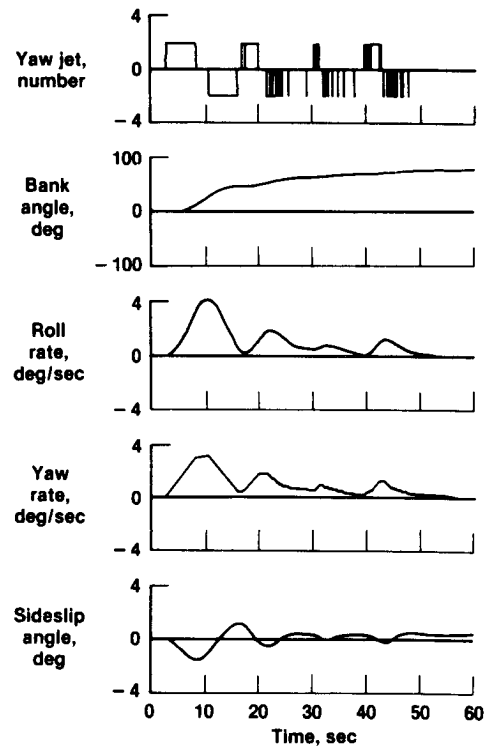
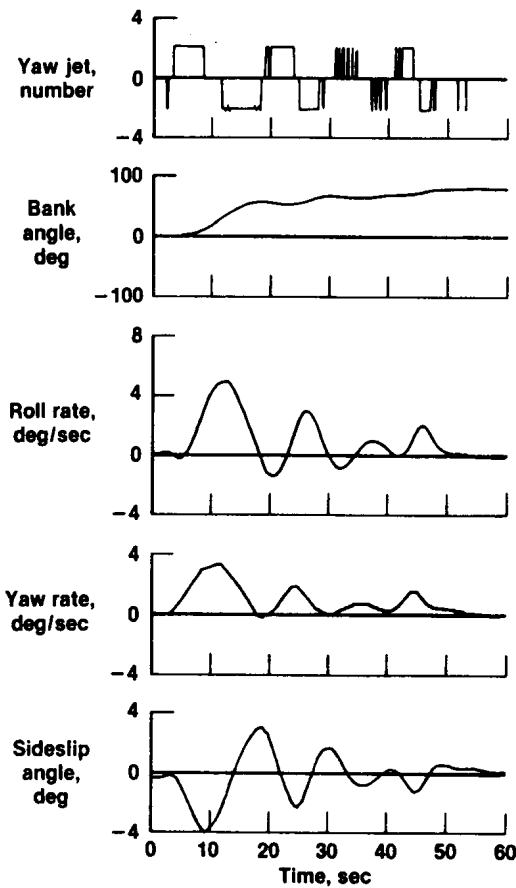
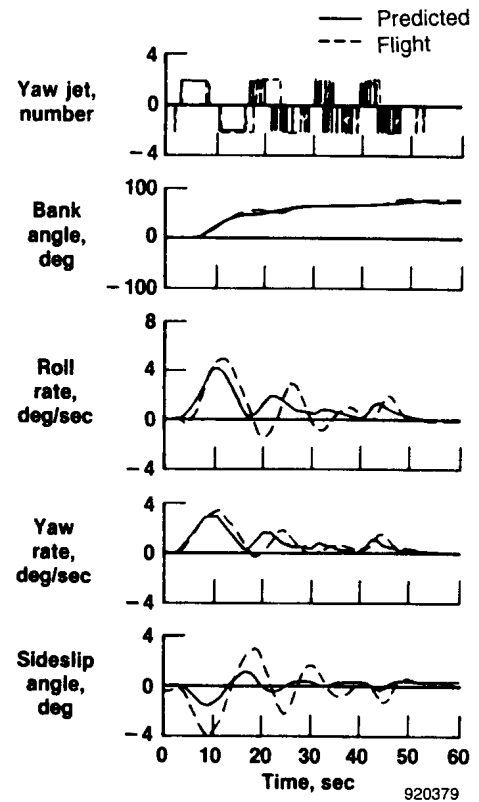


Figure 2. Predicted STS-1 bank maneuver at $V = 24,300$ ft/sec.



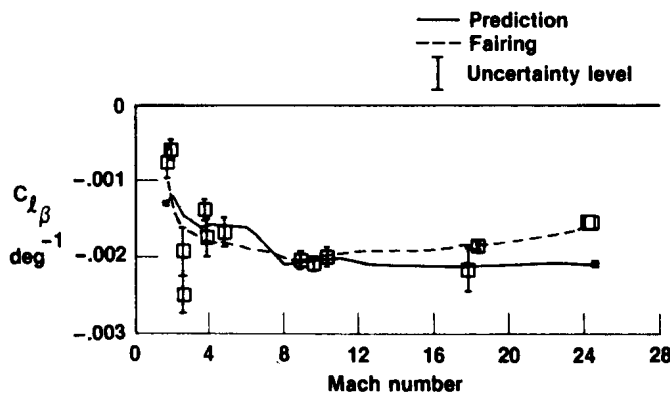
6052

Figure 3. Actual STS-1 bank maneuver at $V = 24,300$ ft/sec.



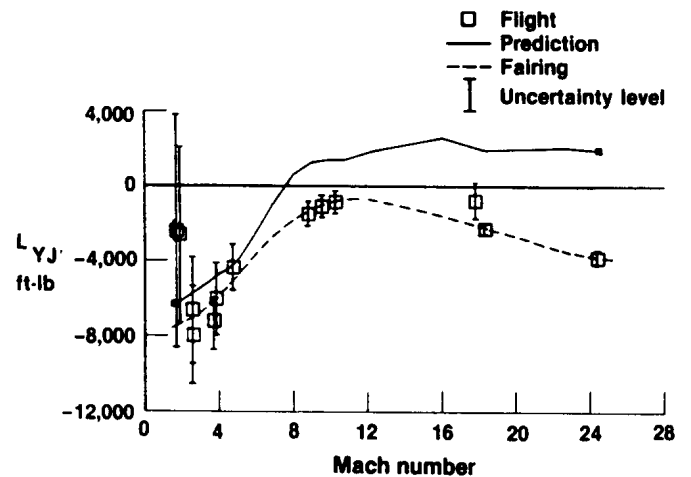
920379

Figure 4. Comparison of actual and predicted STS-1 bank maneuver at $V = 24,300$ ft/sec.



6054

Figure 5. Estimates of $C_{l_{\beta}}$ for the Space Shuttle Orbiter.



6055

Figure 6. Estimates of L_{YJ} for the Space Shuttle Orbiter.

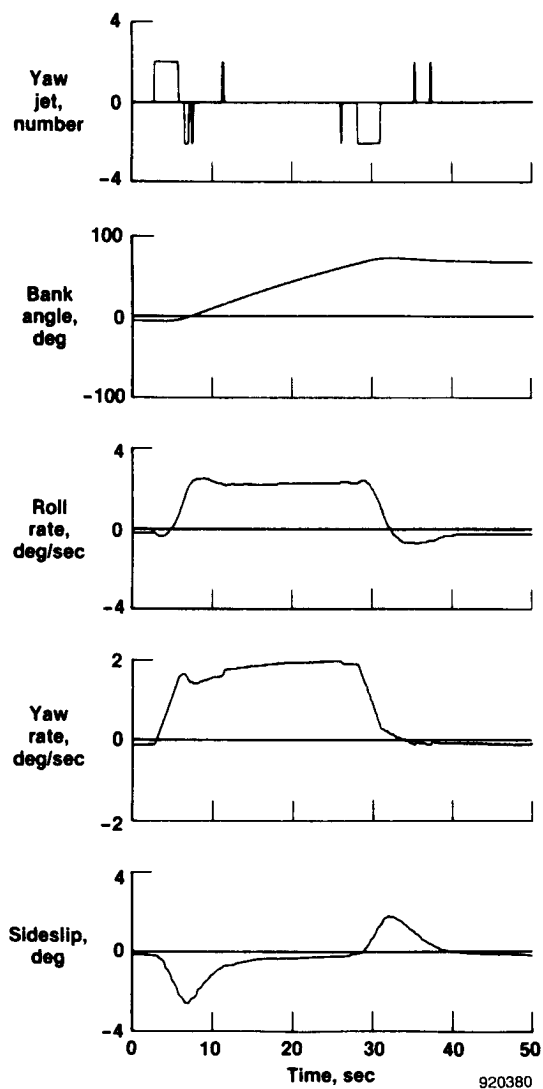


Figure 7. Comparison of simulated bank maneuver with L_{YJ} at a flight-estimated value with the actual STS-1 bank maneuver.

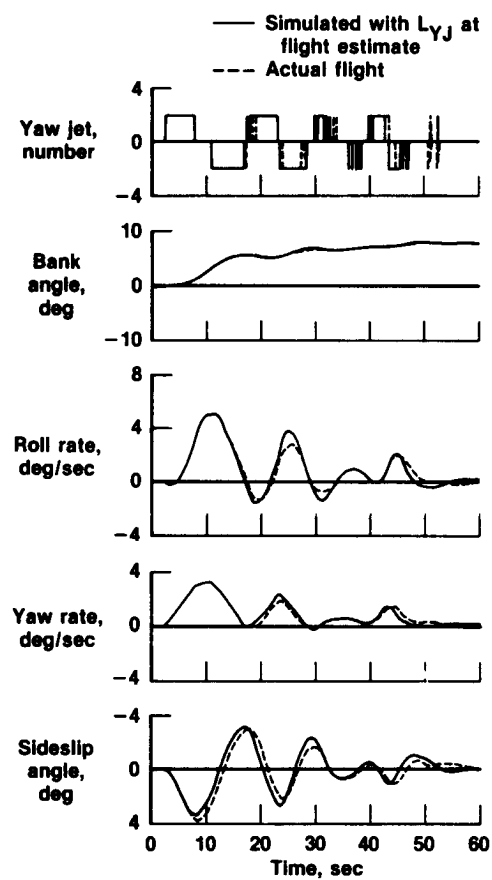
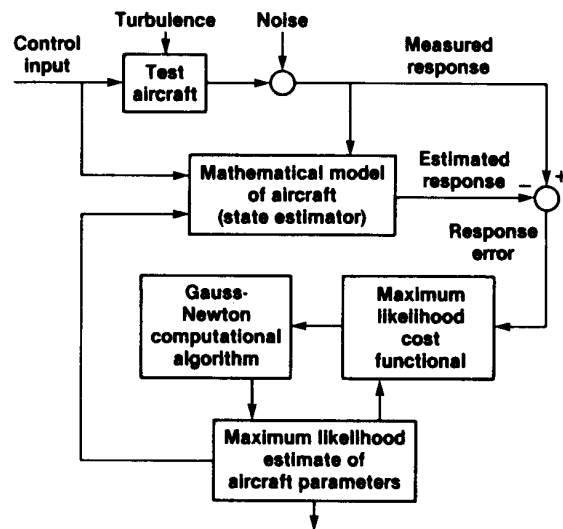
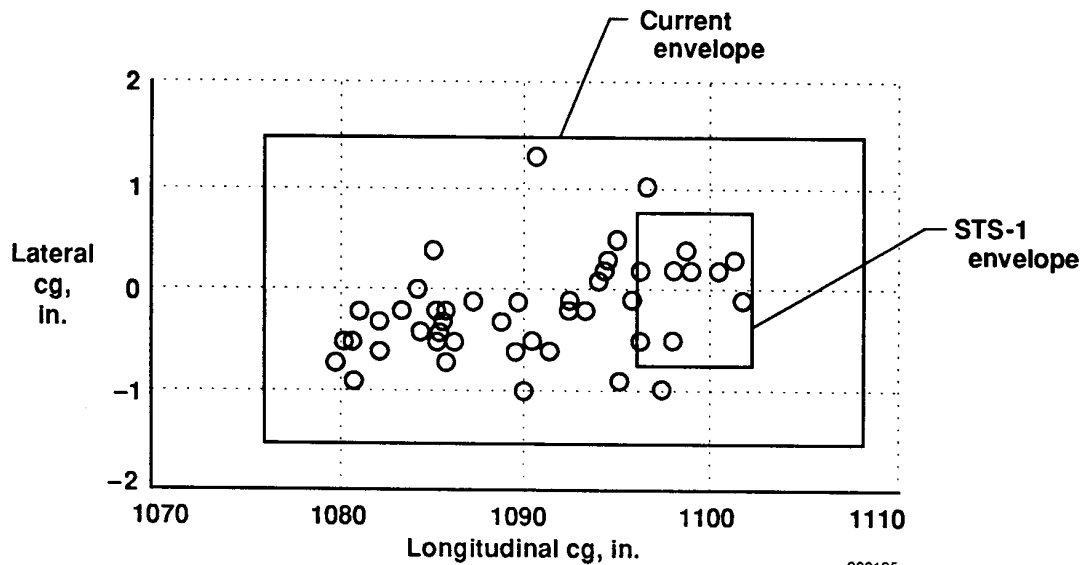


Figure 8. Manual bank maneuver at $V = 24,000$ ft/sec from STS-2.



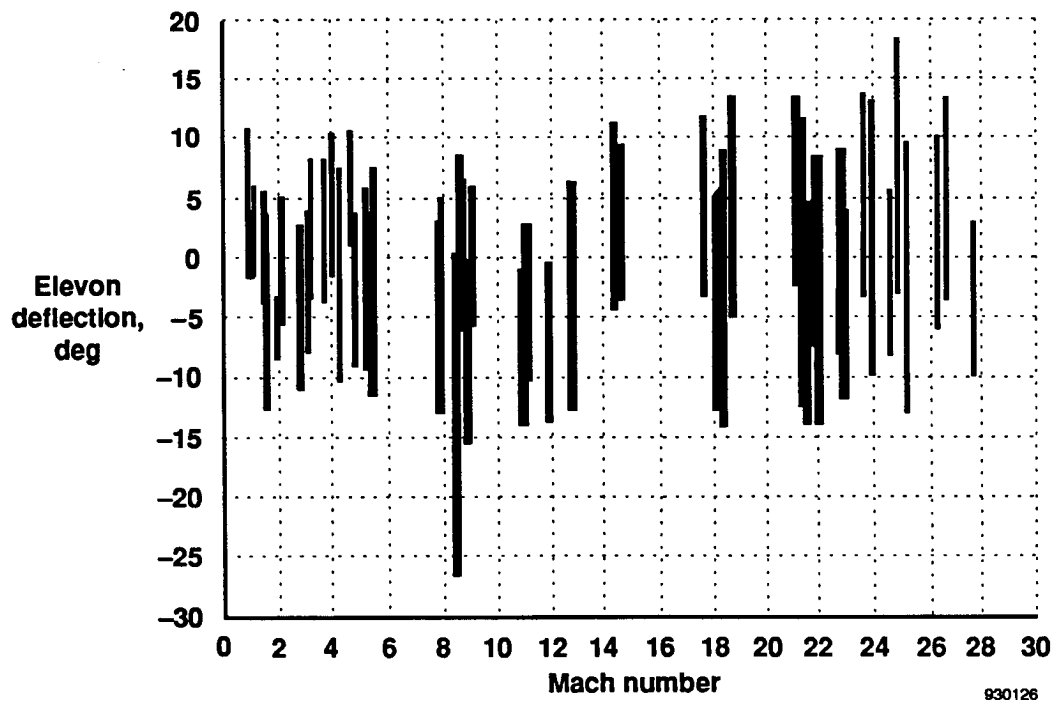
6021

Figure 9. Maximum likelihood estimation concept.

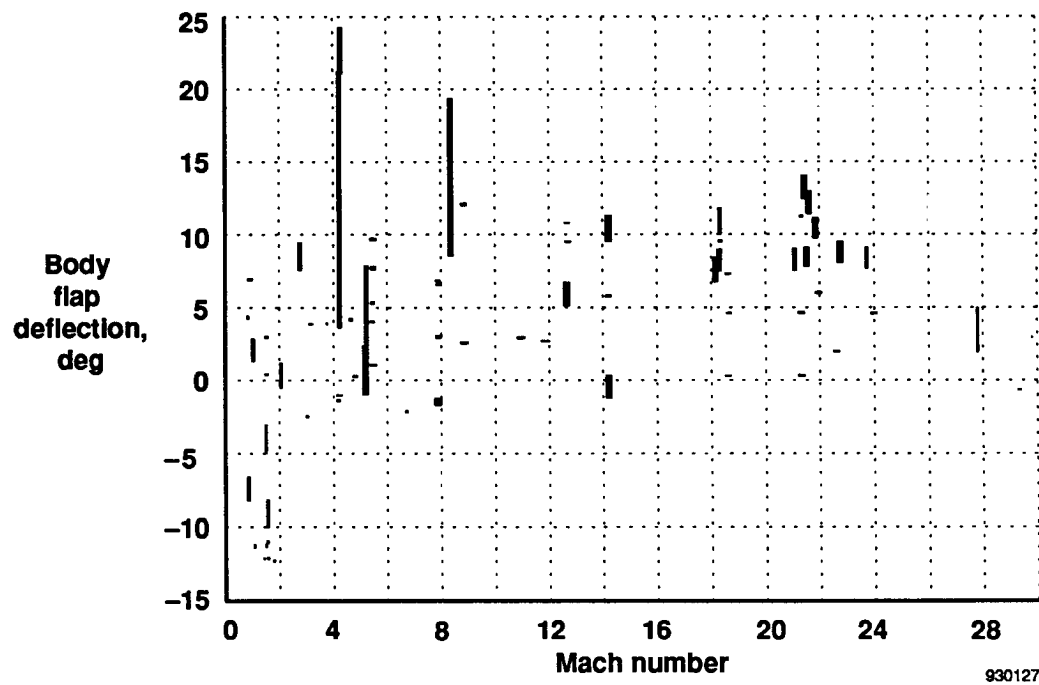


930125

Figure 10. Orbiter center of gravity at entry interface (400,000 ft).

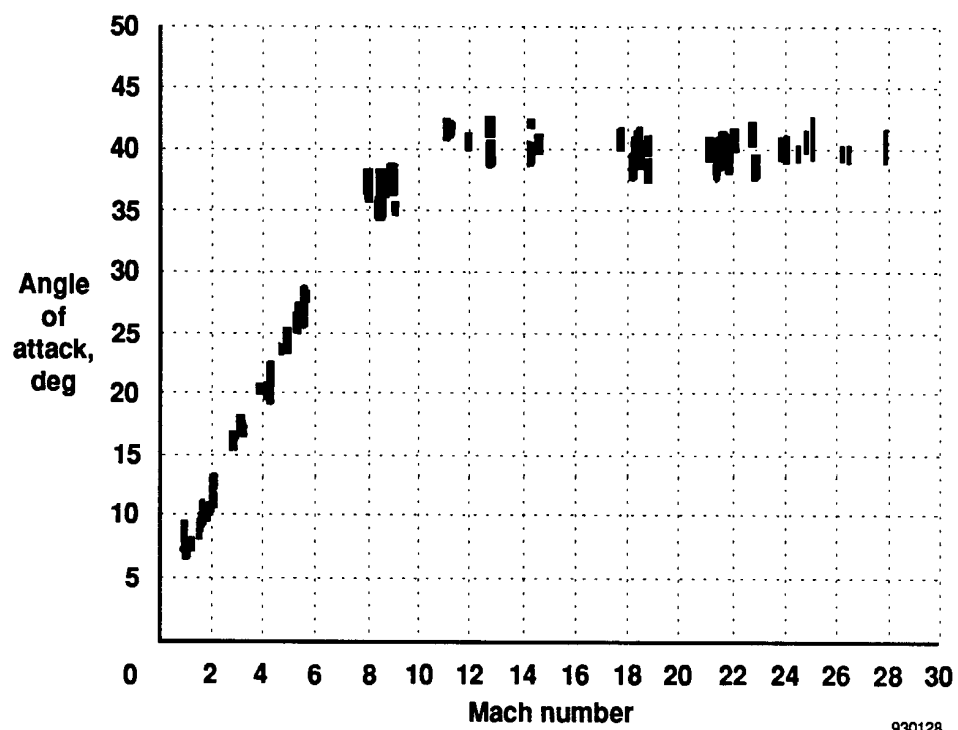


(a) Elevon deflection.



(b) Body flap deflection.

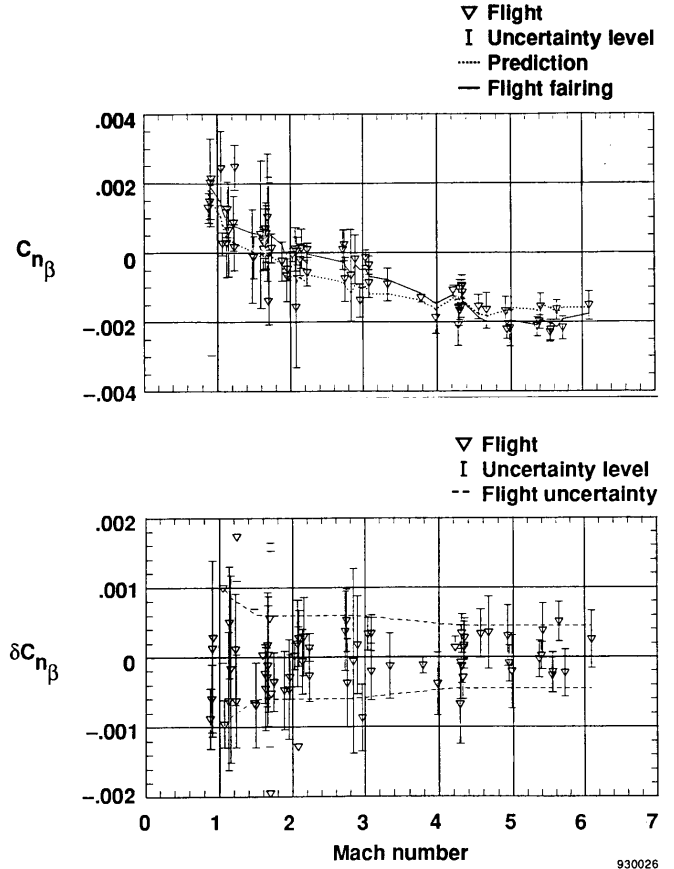
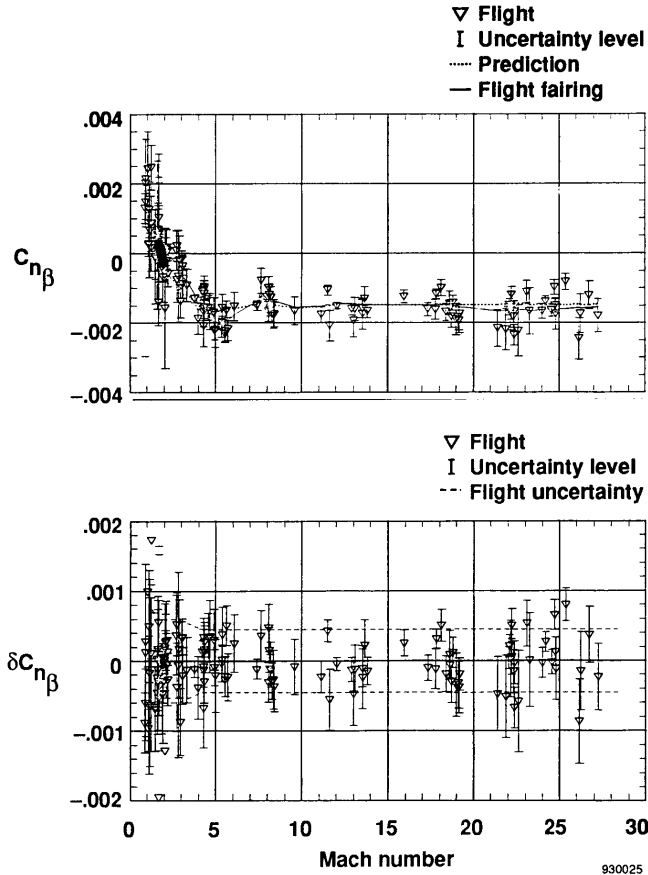
Figure 11. Variations of elevon deflection, body flap deflection, and angle of attack as a function of Mach number.



930128

(c) Angle of attack.

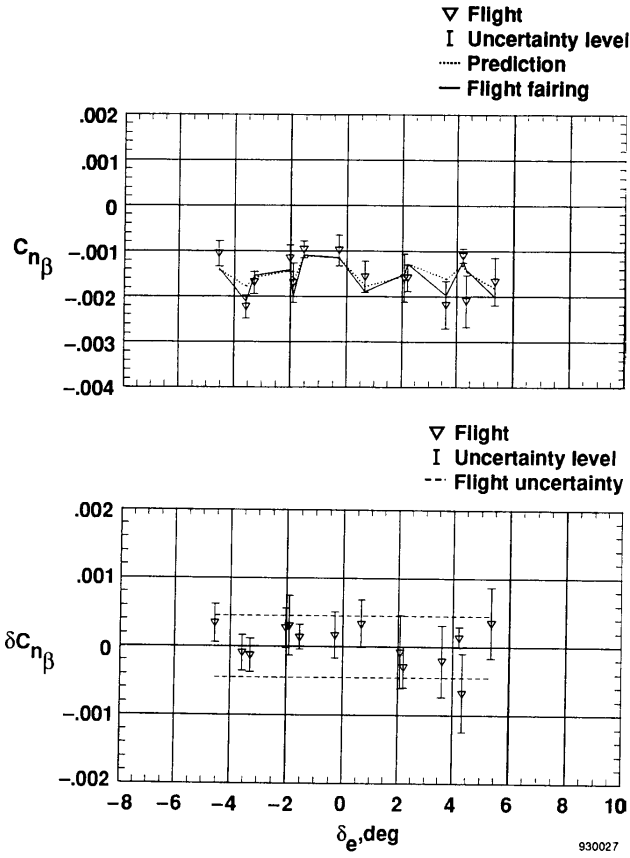
Figure 11. Concluded.



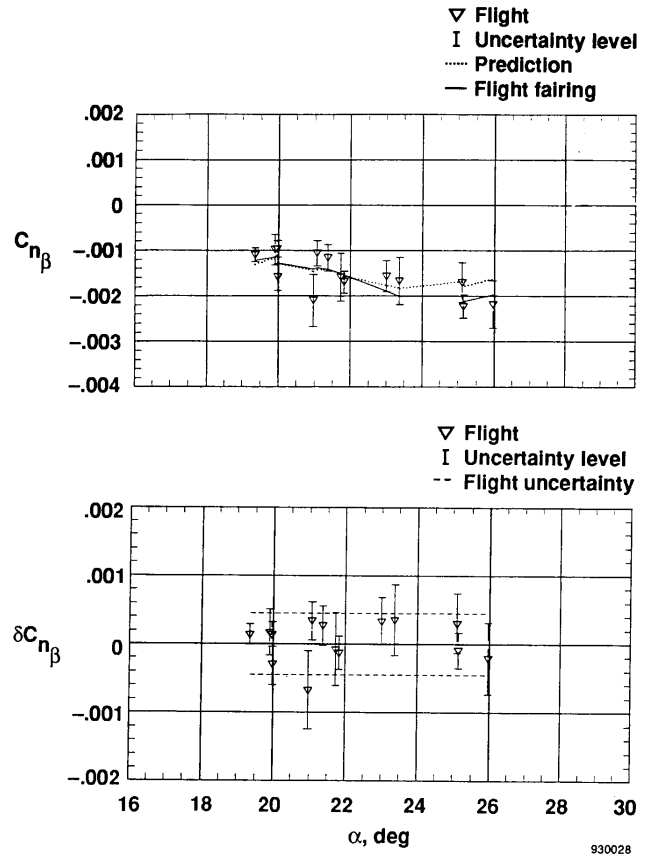
(a) The C_{n_β} and δC_{n_β} as a function of Mach number.

(b) The C_{n_β} and δC_{n_β} as a function of Mach number, $M \leq 7$.

Figure 12. Directional stability, C_{n_β} .



(c) The C_{n_β} and δC_{n_β} as a function of elevon position, δ_e , $4 \leq M \leq 5$.



(d) The C_{n_β} and δC_{n_β} as a function of α , $4 \leq M \leq 5$.

Figure 12. Concluded.

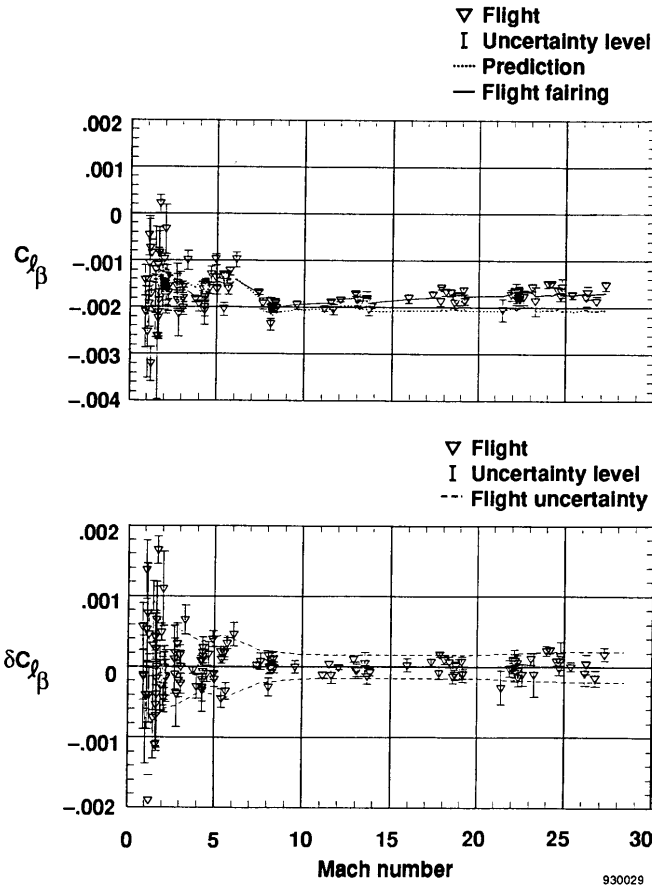
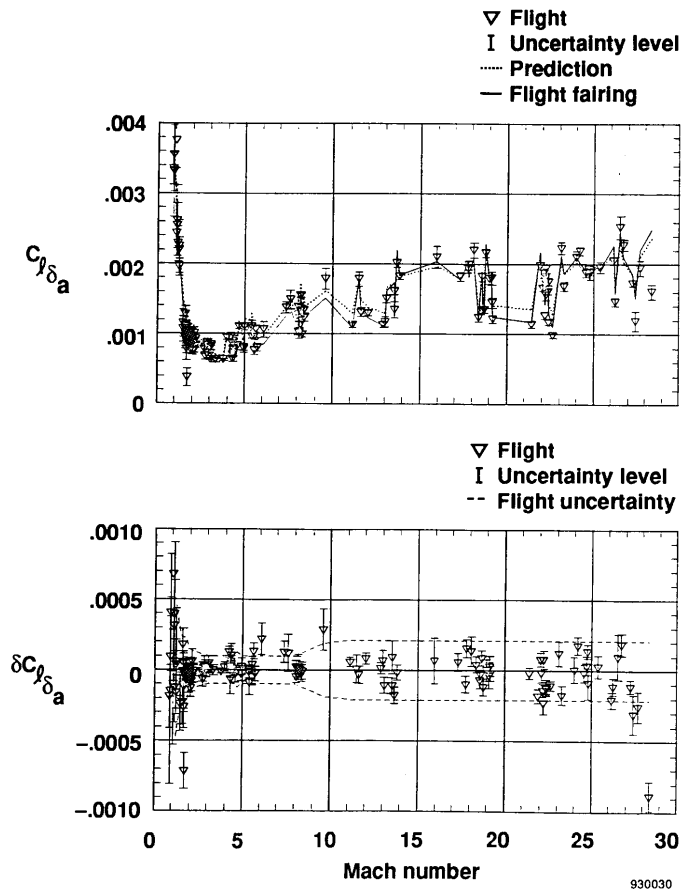
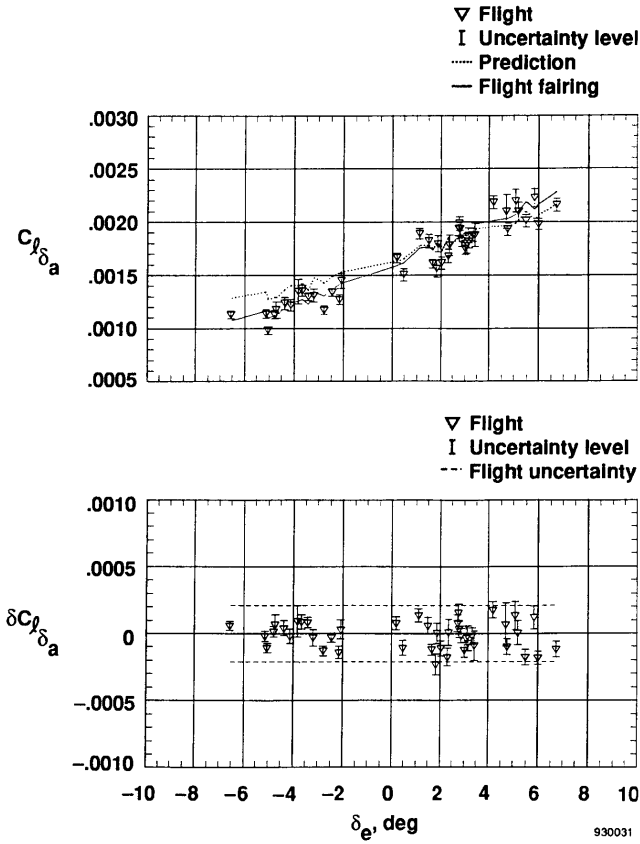


Figure 13. Dihedral effect, $C_{l_{\beta}}$, as a function of Mach number.



(a) The $C_{l_{\delta a}}$ and $\delta C_{l_{\delta a}}$ as a function of Mach number.

Figure 14. Roll control power, $C_{l_{\delta a}}$.



(b) The $C_{l\delta_a}$ and $\delta C_{l\delta_a}$ as a function of elevon position, δ_e , $10 \leq M \leq 25$.

Figure 14. Concluded.

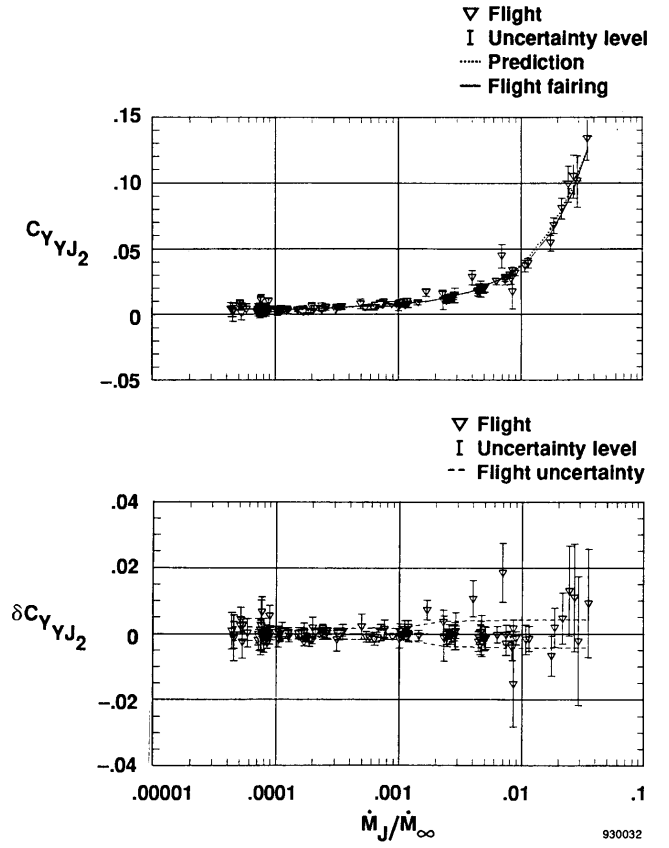


Figure 15. Coefficient of side force due to two yaw jets, C_{YJ_2} , as a function of mass-flow ratio, \dot{M}_J/\dot{M}_∞ .

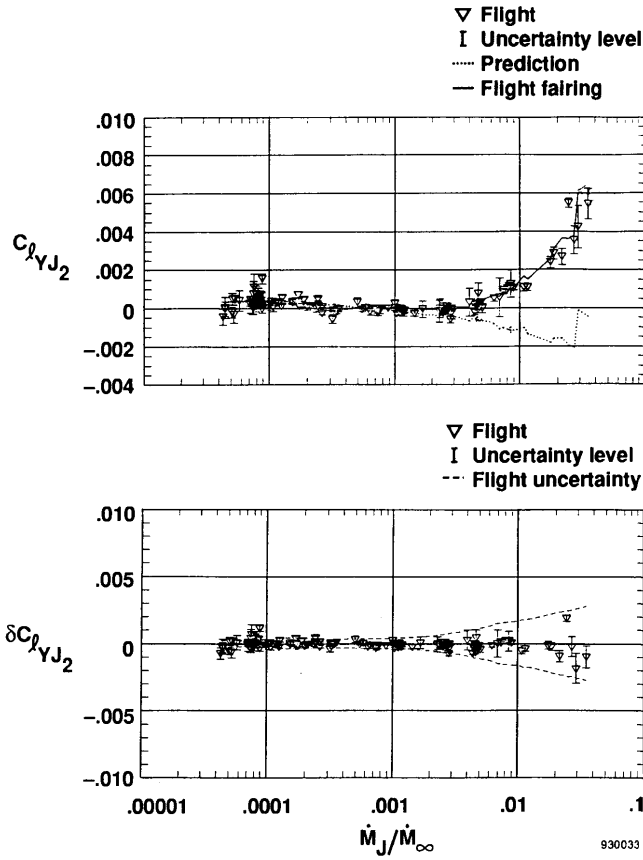


Figure 16. Coefficient of rolling moment due to two yaw jets, $C_{l_{YJ_2}}$, as a function of mass-flow ratio, \dot{M}_J/\dot{M}_∞ .

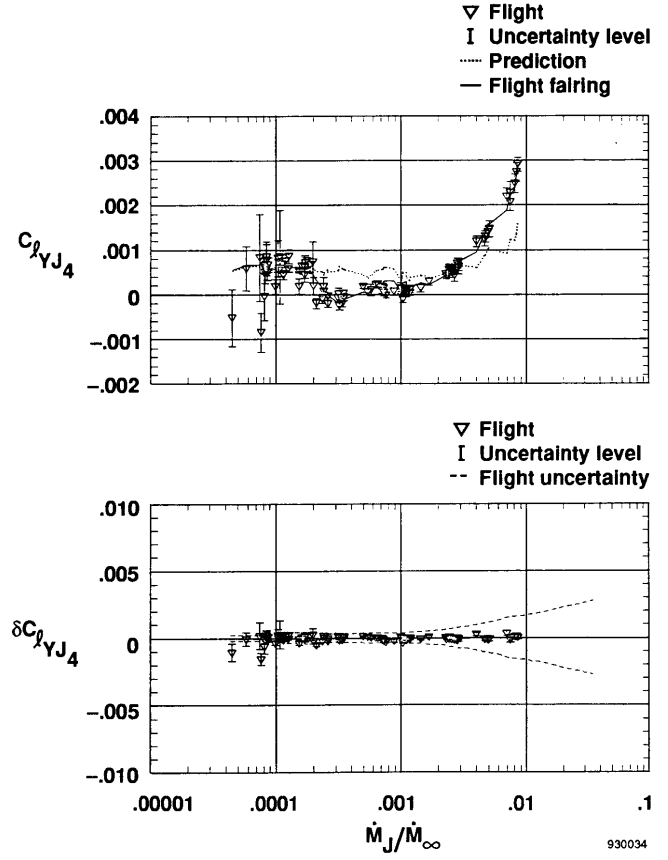


Figure 17. Coefficient of rolling moment due to four yaw jets, $C_{l_{YJ_4}}$, as a function of mass-flow ratio, \dot{M}_J/\dot{M}_∞ .

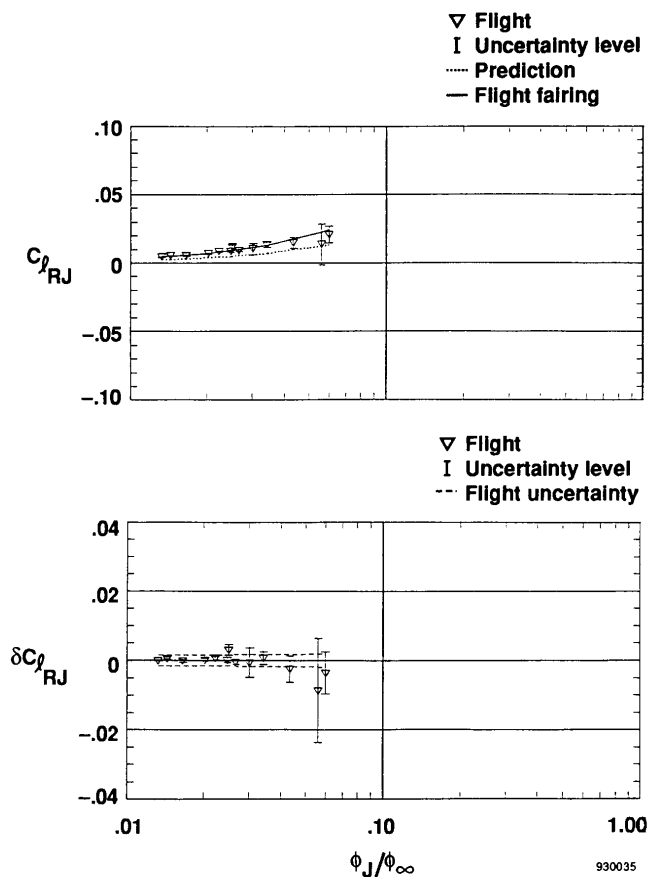


Figure 18. Coefficient of rolling moment due to roll jets, $C_{l_{RJ}}$, as a function of jet momentum ratio, ϕ_J/ϕ_∞ .

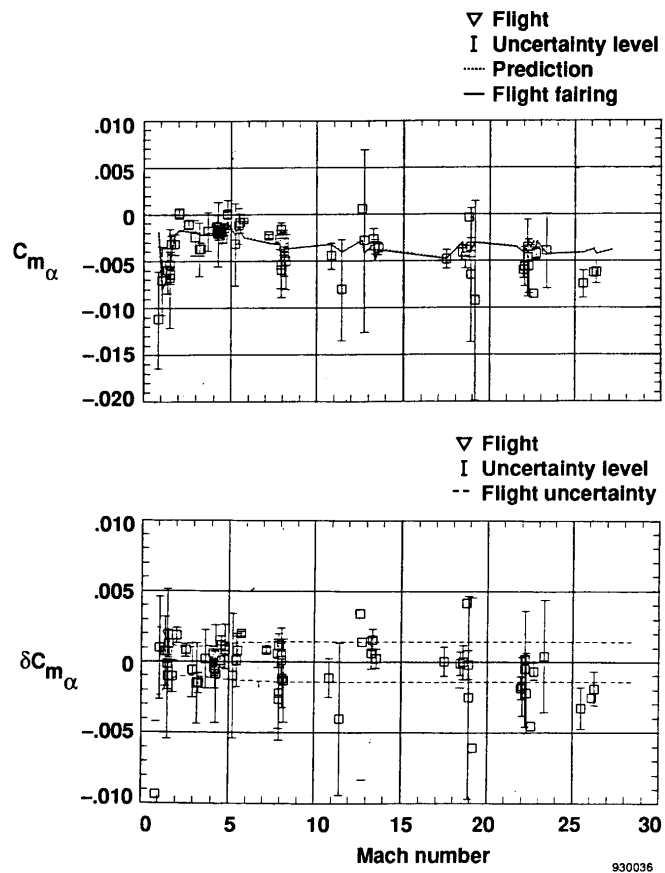


Figure 19. Longitudinal stability term, C_{m_α} , as a function of Mach number, M .

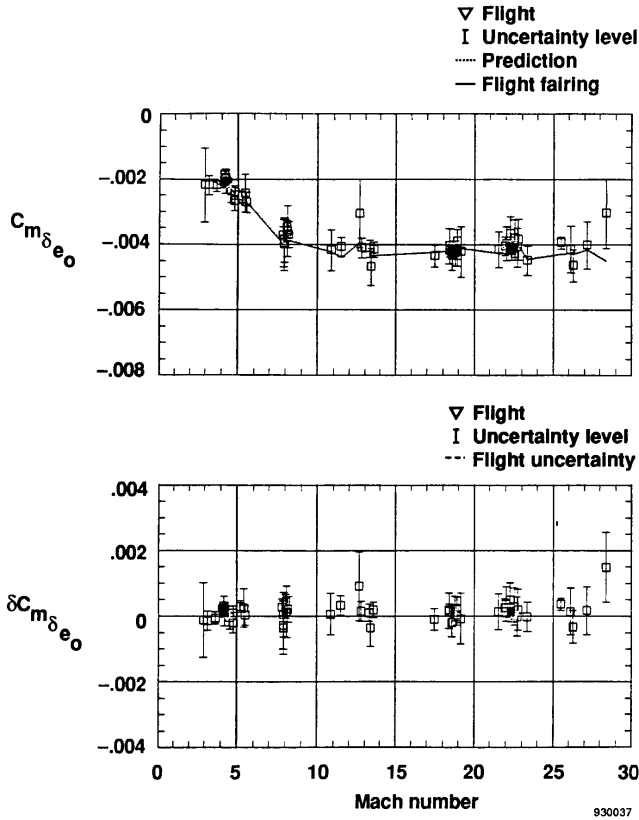


Figure 20. Coefficient of pitching moment due to elevon position, $C_{m_{\delta_{e_0}}}$, as a function of Mach number, M .

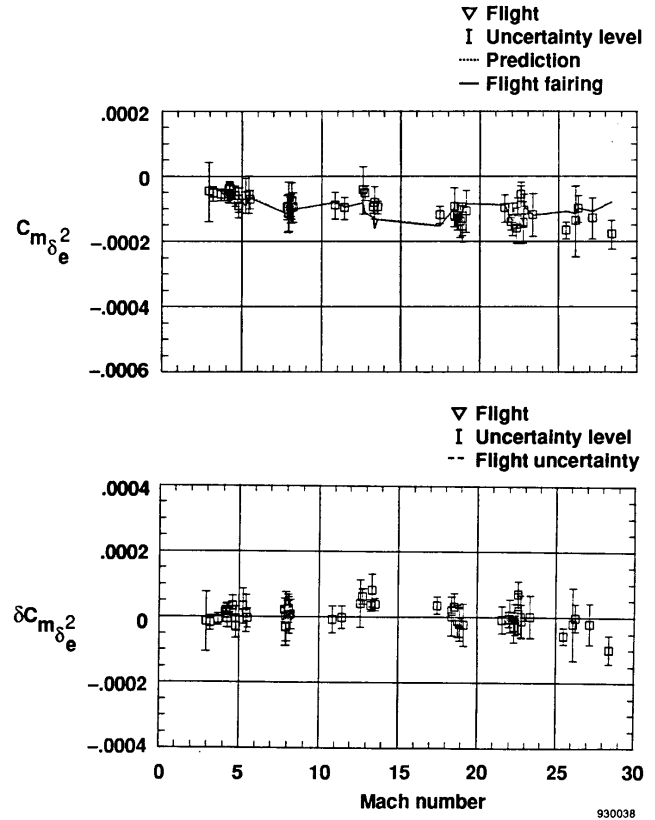


Figure 21. Coefficient of pitching moment due to elevon position squared, $C_{m_{\delta_e^2}}$, as a function of Mach number, M .

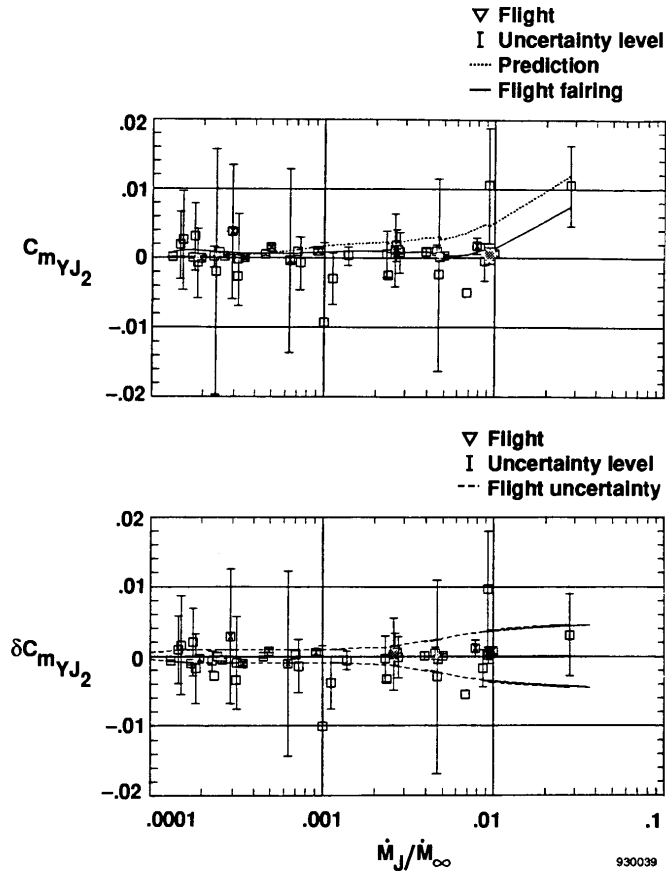


Figure 22. Coefficient of pitching moment due to two yaw jets, $C_{m_{YJ_2}}$, as a function of mass-flow ratio, \dot{M}_J/\dot{M}_∞ .

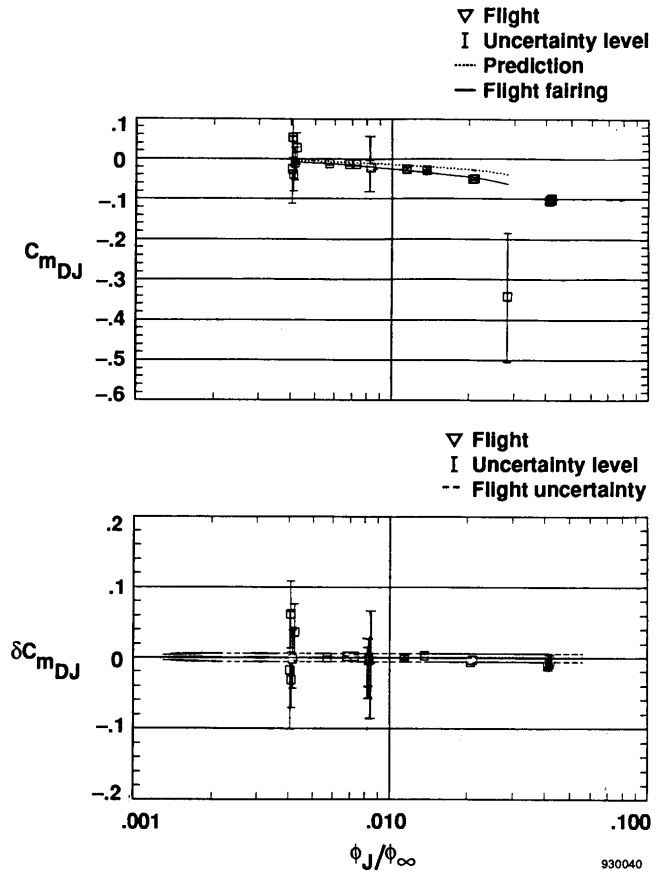


Figure 23. Coefficient of pitching moment due to down-firing jets, $C_{m_{DJ}}$, as a function of mass-flow ratio, \dot{M}_J/\dot{M}_∞ .

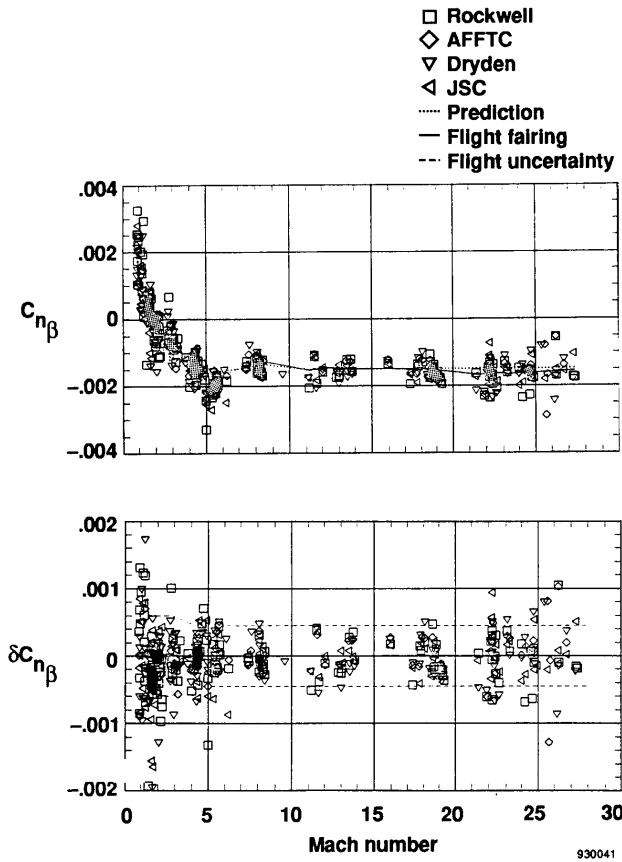
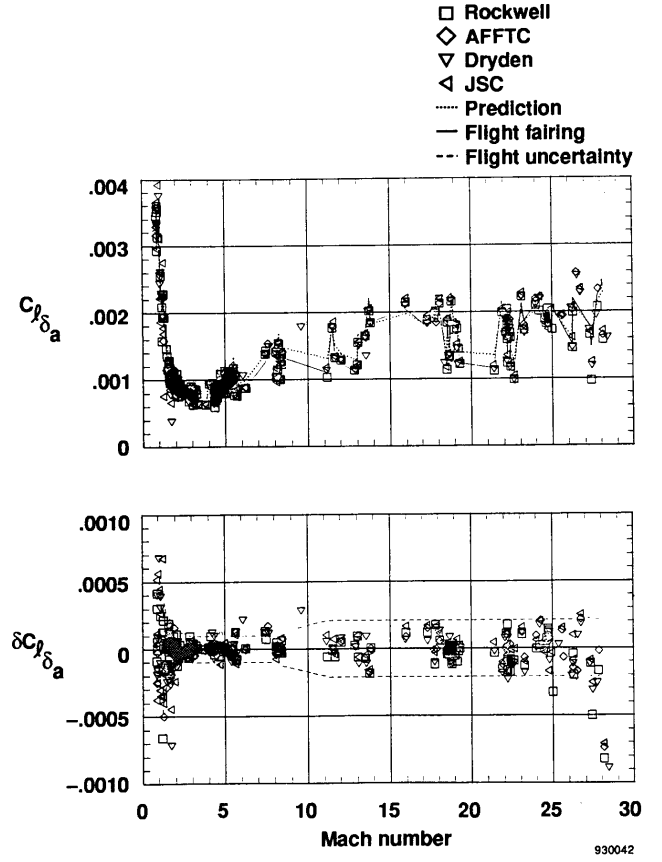
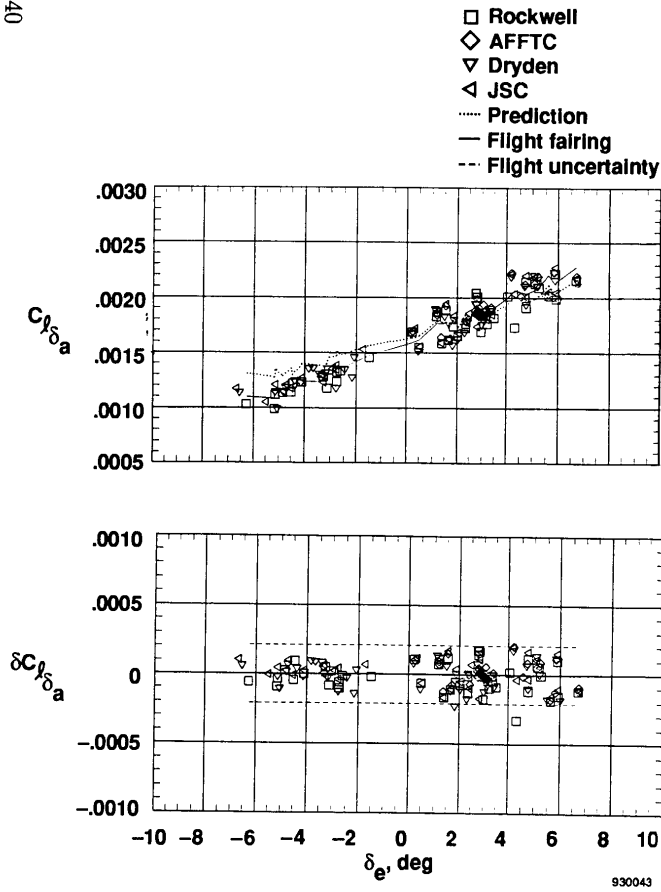


Figure 24. Directional stability, $C_{n\beta}$, as a function of Mach number, M .



(a) The $C_{l\delta_a}$ and $\delta C_{l\delta_a}$ as a function of Mach number.

Figure 25. Roll control power, $C_{l\delta_a}$, from all sets of analysts.



(b) The $C_{l\delta_a}$ and $\delta C_{l\delta_a}$ as a function of elevon position, δ_e , $10 \leq M \leq 25$.

Figure 25. Concluded.

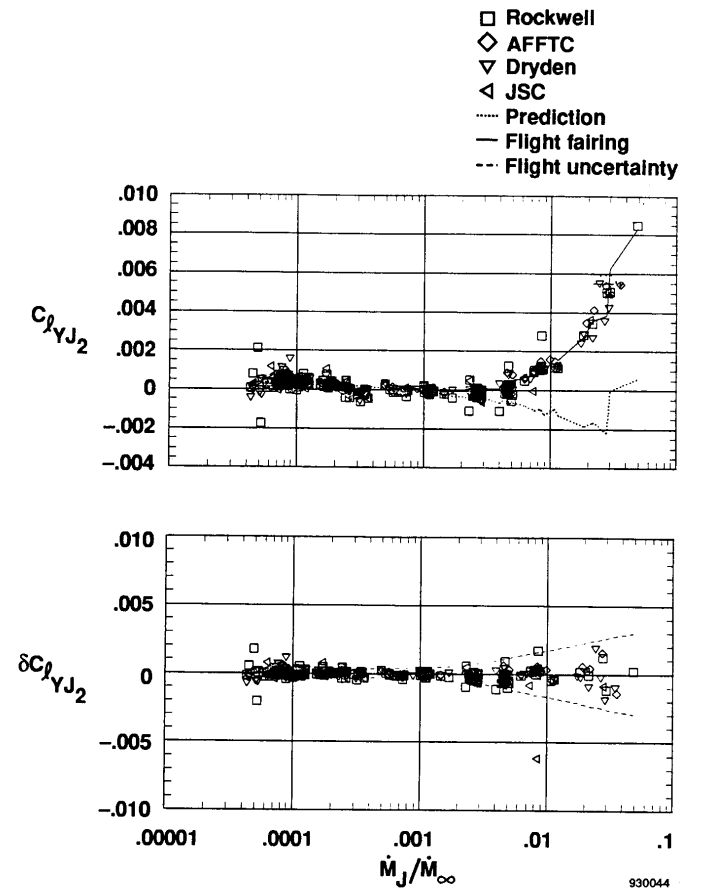
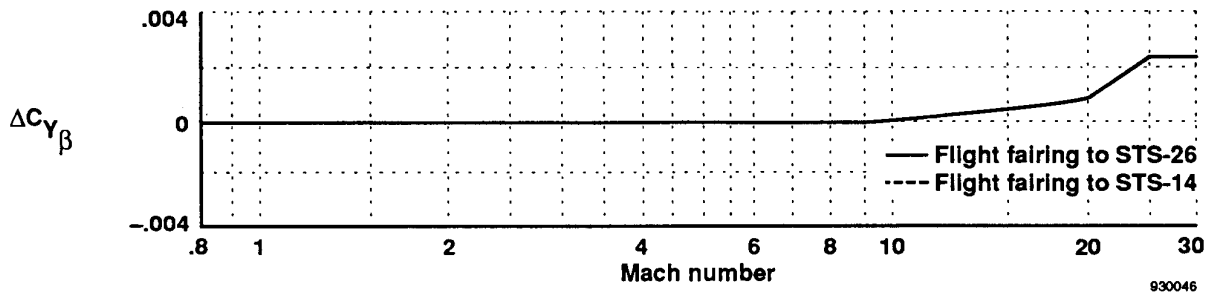
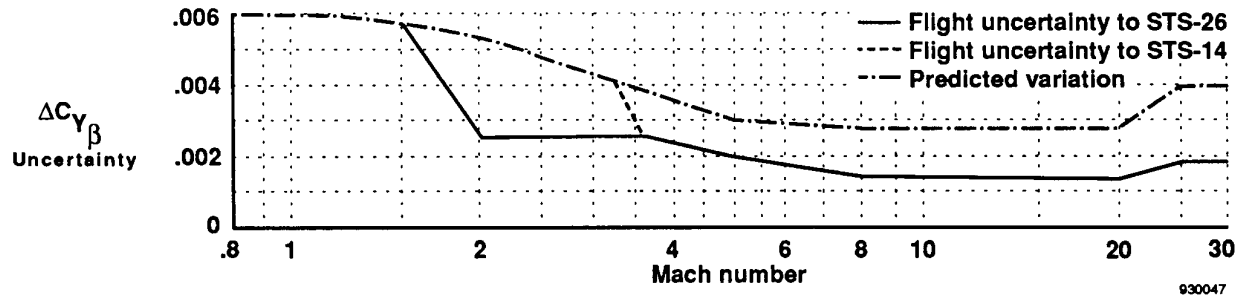


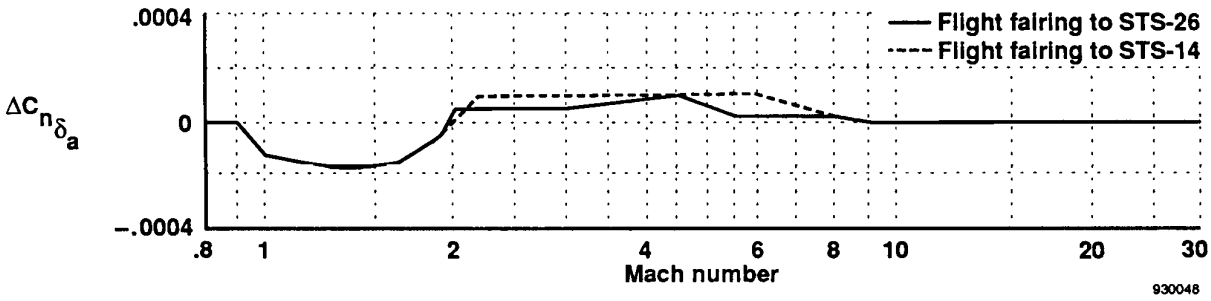
Figure 26. Coefficient of rolling moment due to two yaw jets, C_{lYJ_2} , as a function of mass flow ratio, \dot{M}_J/\dot{M}_∞ .



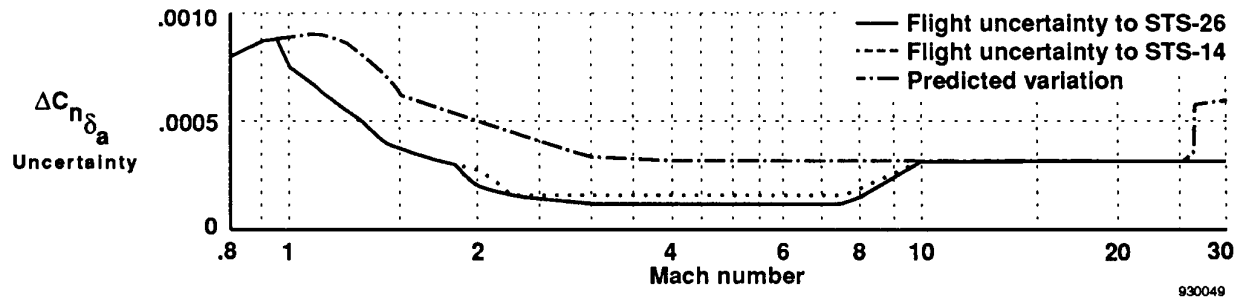
(a) Fairings of ΔC_{Y_β} as a function of Mach number.



(b) Fairings of ΔC_{Y_β} uncertainty as a function of Mach number.

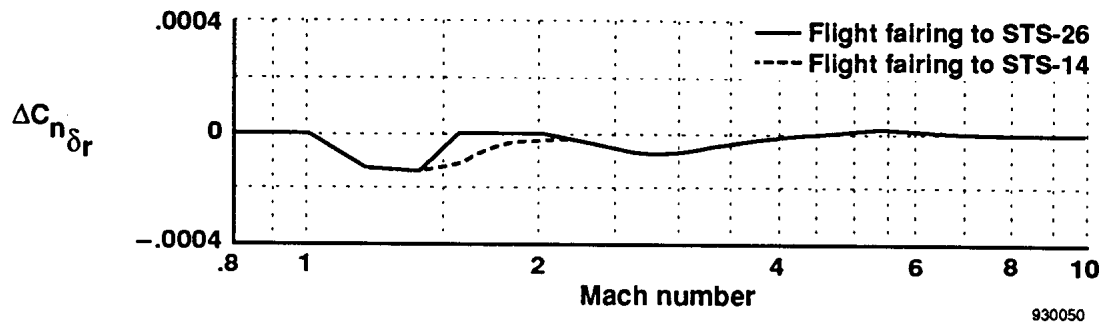


(c) Fairings of $\Delta C_{n_{\delta_a}}$ as a function of Mach number.

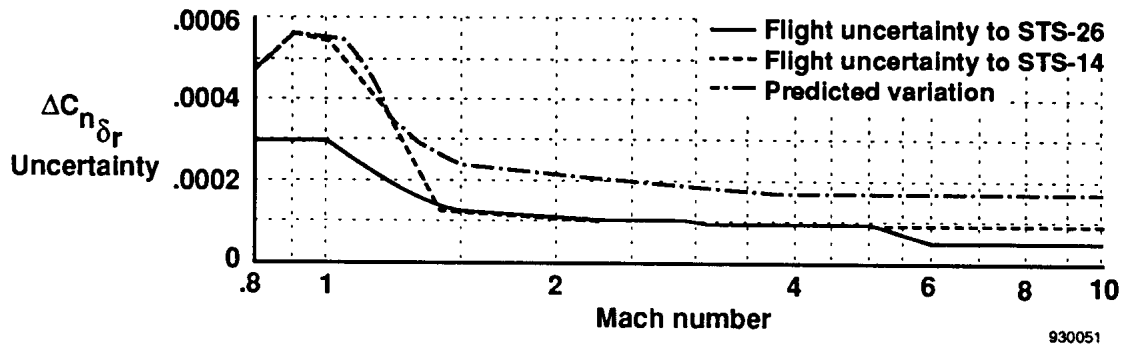


(d) Fairings of $\Delta C_{n_{\delta_a}}$ uncertainty as a function of Mach number.

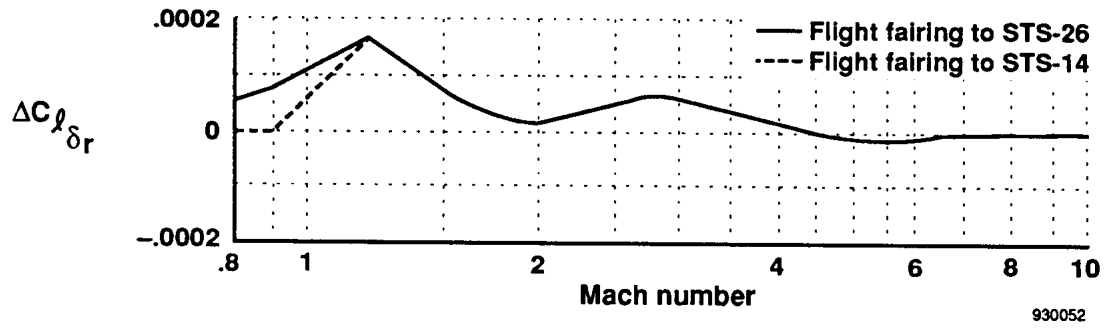
Figure 27. The FAD-14 and FAD-26 fairings.



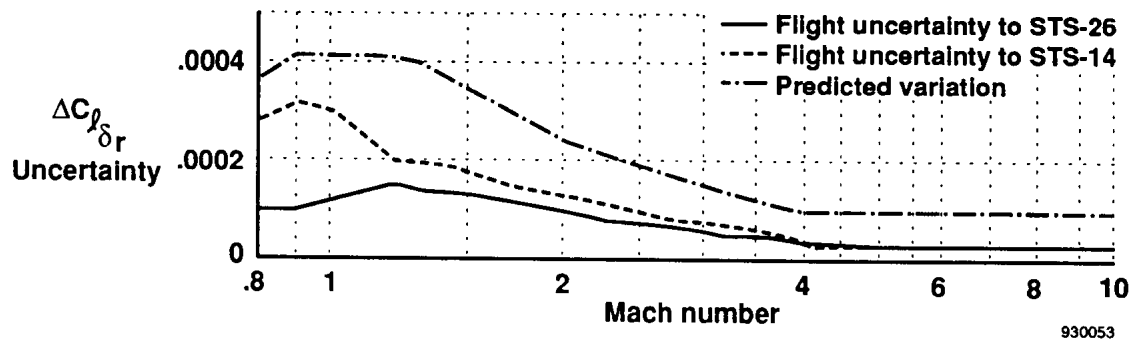
(e) Fairings of $\Delta C_{n_{\delta r}}$ as a function of Mach number.



(f) Fairings of $\Delta C_{n_{\delta r}}$ uncertainty as a function of Mach number.

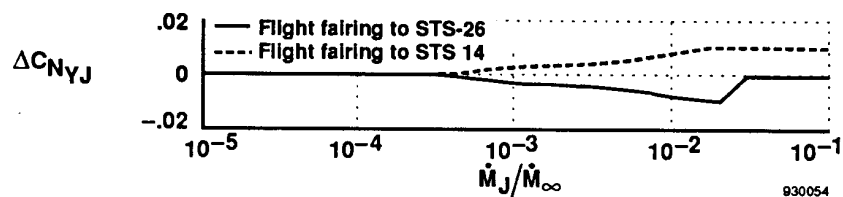


(g) Fairings of $\Delta C_{l_{\delta r}}$ as a function of Mach number.

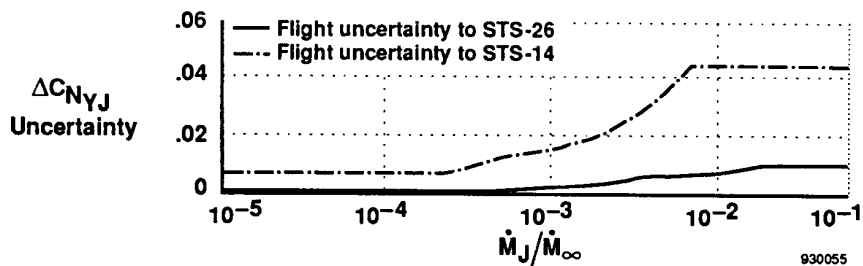


(h) Fairings of $\Delta C_{l_{\delta r}}$ uncertainty as a function of Mach number.

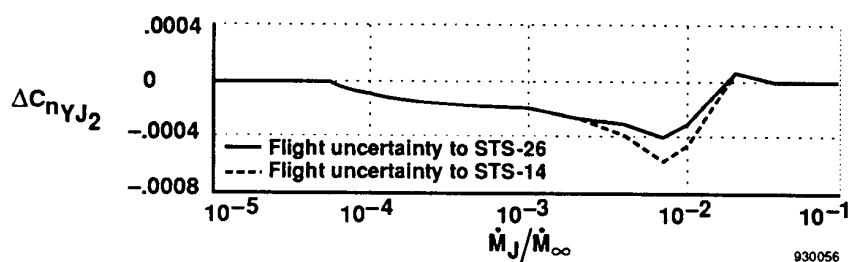
Figure 27. Continued.



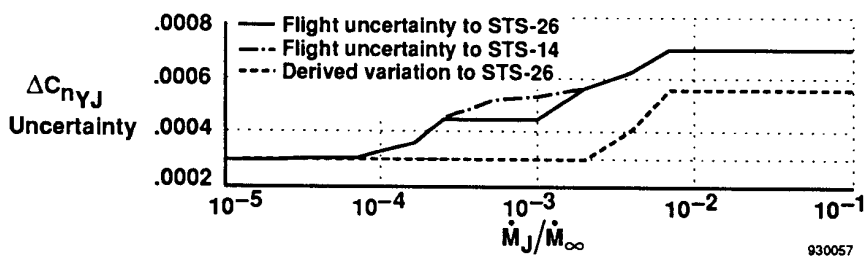
(i) Fairings of $\Delta C_{N_{YJ}}$ as a function of \dot{M}_J/\dot{M}_∞ .



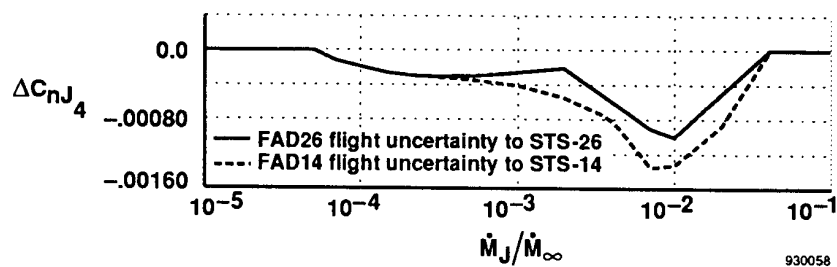
(j) Fairings of $\Delta C_{N_{YJ}}$ uncertainty as a function of \dot{M}_J/\dot{M}_∞ .



(k) Fairings of $\Delta C_{n_{YJ_2}}$ as a function of \dot{M}_J/\dot{M}_∞ .

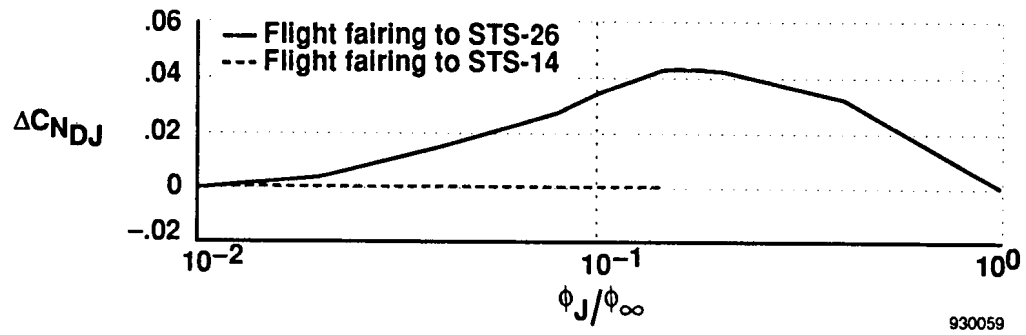


(l) Fairings of $\Delta C_{n_{YJ}}$ uncertainty as a function of \dot{M}_J/\dot{M}_∞ .

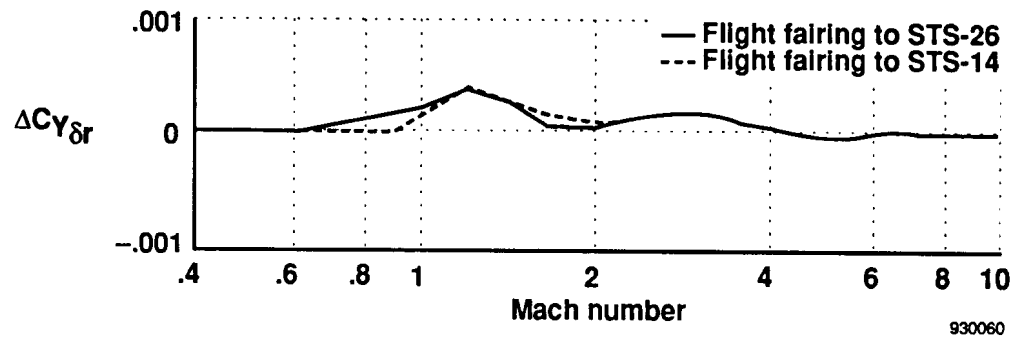


(m) Fairings of $\Delta C_{n_{YJ_4}}$ as a function of \dot{M}_J/\dot{M}_∞ .

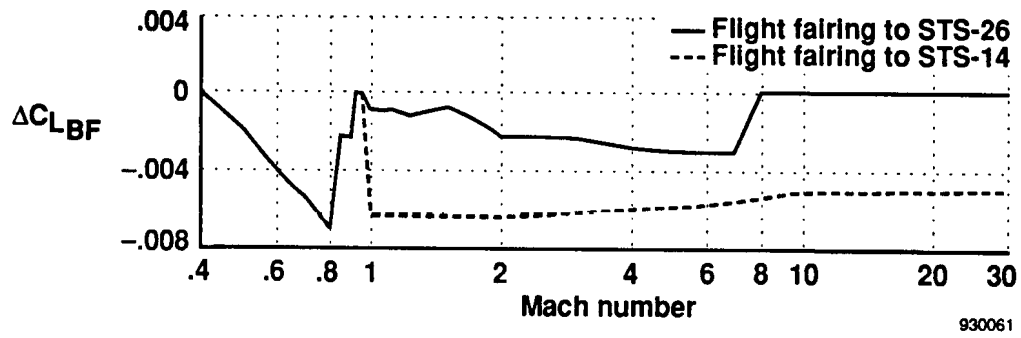
Figure 27. Continued.



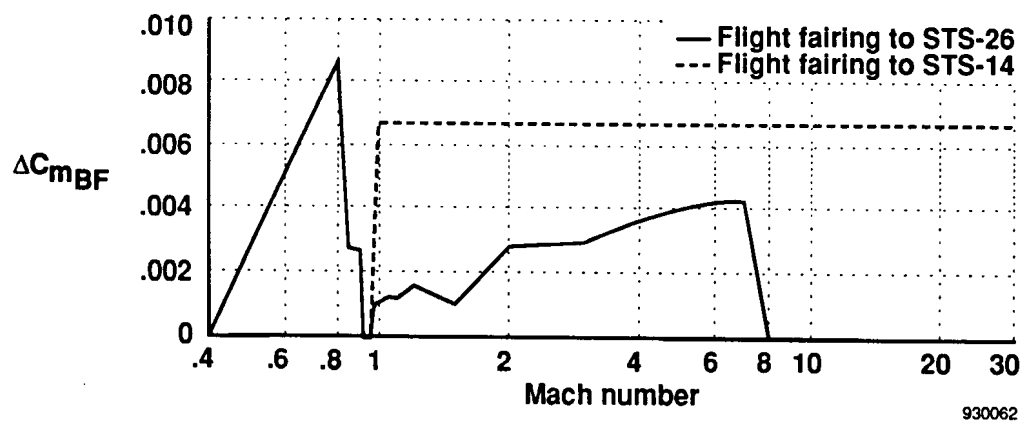
(n) Fairings of $\Delta C_{N_{DJ}}$ as a function of ϕ_J/ϕ_∞ .



(o) Fairings of $\Delta C_{Y_{\delta r}}$ as a function of Mach number.



(p) Fairings of $\Delta C_{L_{BF}}$ as a function of Mach number.



(q) Fairings of $\Delta C_{m_{BF}}$ as a function of Mach number.

Figure 27. Concluded.

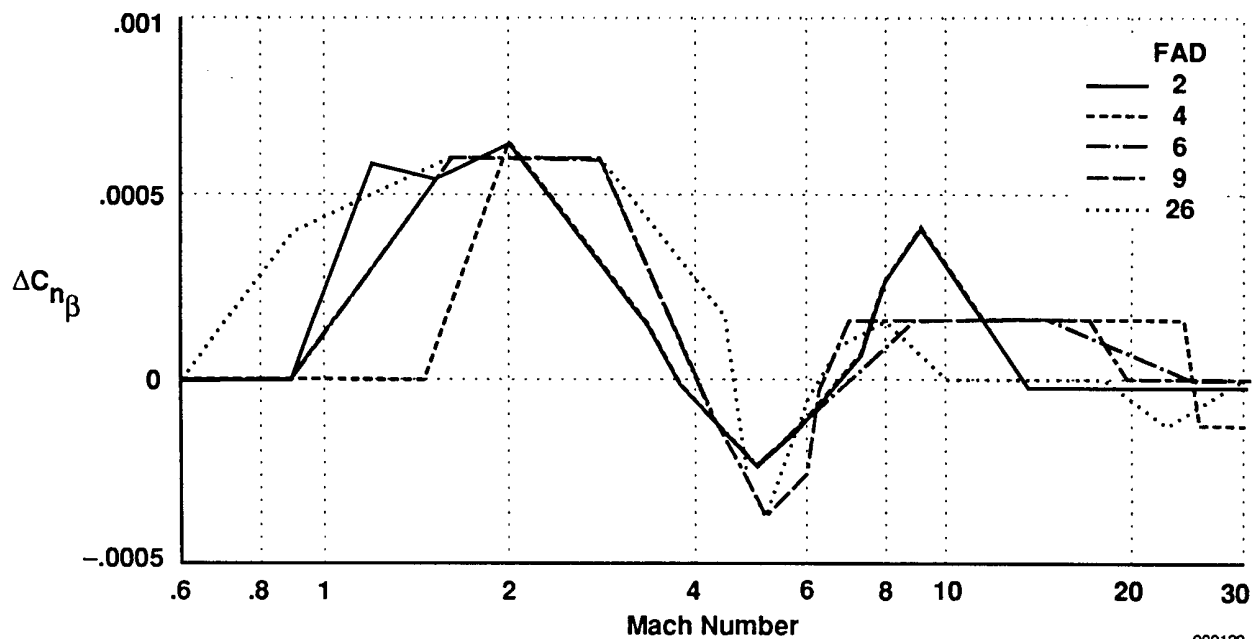


Figure 28. Fairings of $\Delta C_{n\beta}$ as a function of Mach number for several FAD's.

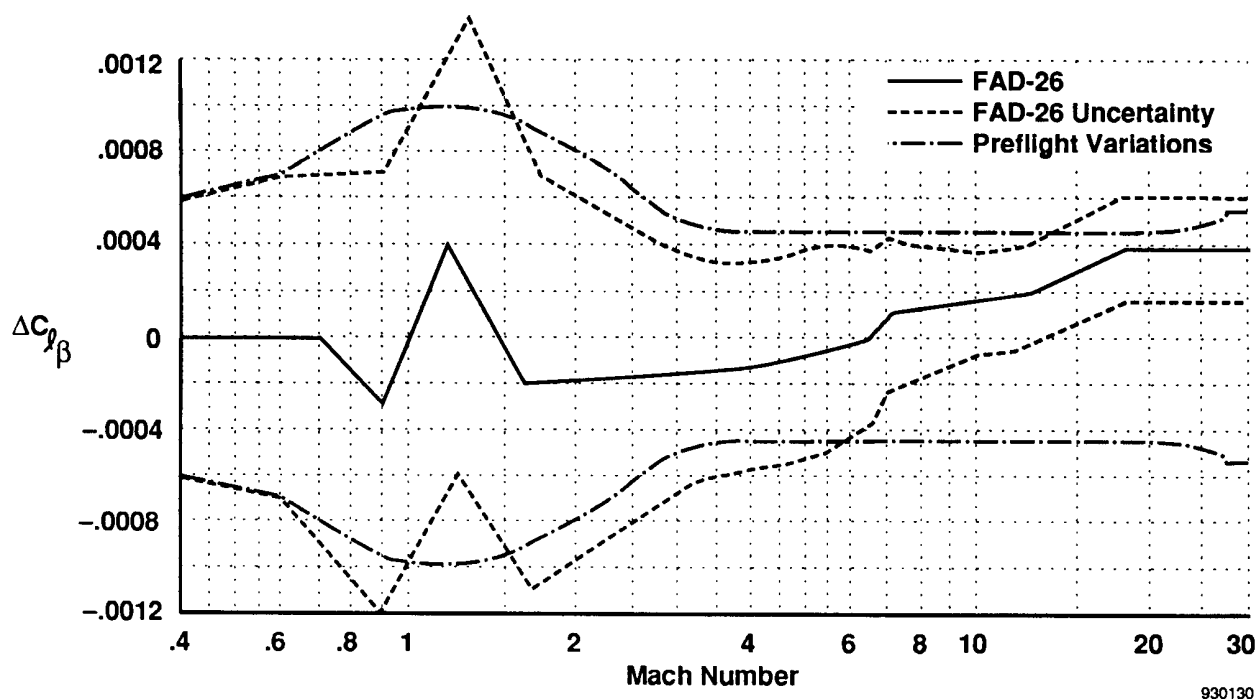
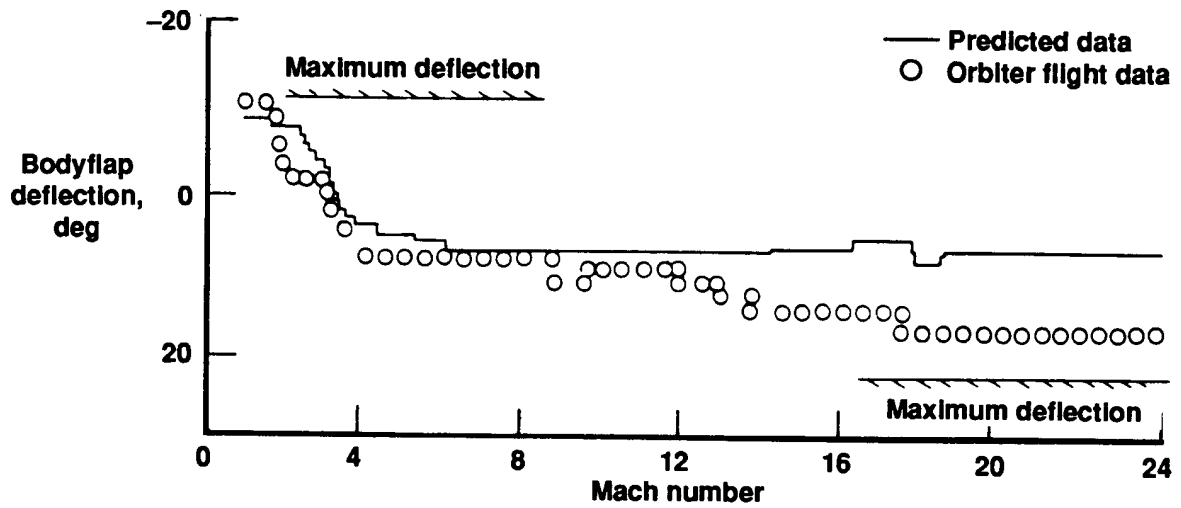
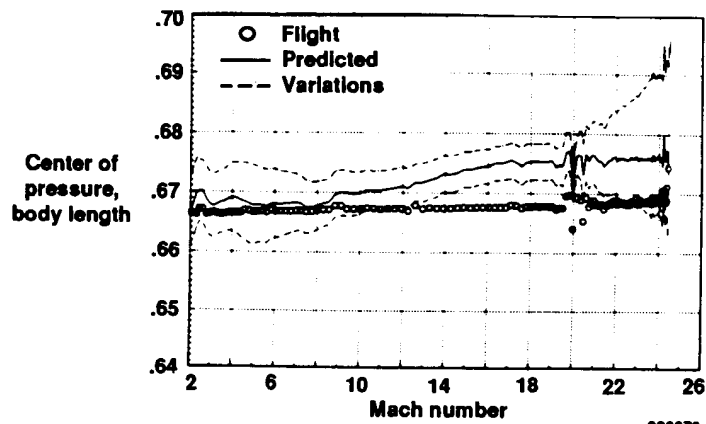


Figure 29. Fairings of $\Delta C_{l\beta}$ as a function of Mach number for FAD-26 and the preflight aerodynamic data book.



920375

Figure 30. Longitudinal trim characteristics from STS-1 (from ref. 14).



920376

Figure 31. The STS-2 longitudinal aerodynamic center-of-pressure location comparison (from ref. 20).